

# A Measurement of the Proton Structure Function $F_2(x, Q^2)$ at Low $x$ and Low $Q^2$ at HERA

H1 Collaboration

## Abstract:

The results of a measurement of the proton structure function  $F_2(x, Q^2)$  and the virtual photon-proton cross section are reported for momentum transfers squared  $Q^2$  between 0.35 GeV<sup>2</sup> and 3.5 GeV<sup>2</sup> and for Bjorken- $x$  values down to  $6 \cdot 10^{-6}$  using data collected by the HERA experiment H1 in 1995. The data represent an increase in kinematic reach to lower  $x$  and  $Q^2$  values of about a factor of 5 compared to previous H1 measurements. Including measurements from fixed target experiments the rise of  $F_2$  with decreasing  $x$  is found to be less steep for the lowest  $Q^2$  values measured. Phenomenological models at low  $Q^2$  are compared with the data.

C. Adloff<sup>35</sup>, S. Aid<sup>13</sup>, M. Anderson<sup>23</sup>, V. Andreev<sup>26</sup>, B. Andrieu<sup>29</sup>, V. Arkadov<sup>36</sup>, C. Arndt<sup>11</sup>,  
 I. Ayyaz<sup>30</sup>, A. Babaev<sup>25</sup>, J. Bähr<sup>36</sup>, J. Bán<sup>18</sup>, Y. Ban<sup>28</sup>, P. Baranov<sup>26</sup>, E. Barrelet<sup>30</sup>, R. Barschke<sup>11</sup>,  
 W. Bartel<sup>11</sup>, U. Bassler<sup>30</sup>, H.P. Beck<sup>38</sup>, M. Beck<sup>14</sup>, H.-J. Behrend<sup>11</sup>, A. Belousov<sup>26</sup>, Ch. Berger<sup>1</sup>,  
 G. Bernardi<sup>30</sup>, G. Bertrand-Coremans<sup>4</sup>, R. Beyer<sup>11</sup>, P. Biddulph<sup>23</sup>, P. Bispham<sup>23</sup>, J.C. Bizot<sup>28</sup>,  
 K. Borrás<sup>8</sup>, F. Botterweck<sup>27</sup>, V. Boudry<sup>29</sup>, S. Bourov<sup>25</sup>, A. Braemer<sup>15</sup>, W. Braunschweig<sup>1</sup>,  
 V. Brisson<sup>28</sup>, W. Brückner<sup>14</sup>, P. Bruel<sup>29</sup>, D. Bruncko<sup>18</sup>, C. Brune<sup>16</sup>, R. Buchholz<sup>11</sup>, L. Büngener<sup>13</sup>,  
 J. Bürger<sup>11</sup>, F.W. Büsler<sup>13</sup>, A. Buniatian<sup>4</sup>, S. Burke<sup>19</sup>, M.J. Burton<sup>23</sup>, G. Buschhorn<sup>27</sup>,  
 D. Calvet<sup>24</sup>, A.J. Campbell<sup>11</sup>, T. Carli<sup>27</sup>, M. Charlet<sup>11</sup>, D. Clarke<sup>5</sup>, B. Clerbaux<sup>4</sup>, S. Cocks<sup>20</sup>,  
 J.G. Contreras<sup>8</sup>, C. Cormack<sup>20</sup>, J.A. Coughlan<sup>5</sup>, A. Courau<sup>28</sup>, M.-C. Cousinou<sup>24</sup>, B.E. Cox<sup>23</sup>,  
 G. Cozzika<sup>9</sup>, D.G. Cussans<sup>5</sup>, J. Cvach<sup>31</sup>, S. Dagoret<sup>30</sup>, J.B. Dainton<sup>20</sup>, W.D. Dau<sup>17</sup>, K. Daum<sup>40</sup>,  
 M. David<sup>9</sup>, C.L. Davis<sup>19,41</sup>, A. De Roeck<sup>11</sup>, E.A. De Wolf<sup>4</sup>, B. Delcourt<sup>28</sup>, M. Dirkmann<sup>8</sup>,  
 P. Dixon<sup>19</sup>, W. Dlugosz<sup>7</sup>, C. Dollfus<sup>38</sup>, K.T. Donovan<sup>21</sup>, J.D. Dowell<sup>3</sup>, H.B. Dreis<sup>2</sup>, A. Drouotkoj<sup>25</sup>,  
 J. Ebert<sup>35</sup>, T.R. Ebert<sup>20</sup>, G. Eckerlin<sup>11</sup>, V. Efremenko<sup>25</sup>, S. Egli<sup>38</sup>, R. Eichler<sup>37</sup>, F. Eisele<sup>15</sup>,  
 E. Eisenhandler<sup>21</sup>, E. Elsen<sup>11</sup>, M. Erdmann<sup>15</sup>, A.B. Fahr<sup>13</sup>, L. Favart<sup>28</sup>, A. Fedotov<sup>25</sup>, R. Felst<sup>11</sup>,  
 J. Feltesse<sup>9</sup>, J. Ferencei<sup>18</sup>, F. Ferrarotto<sup>33</sup>, K. Flamm<sup>11</sup>, M. Fleischer<sup>8</sup>, M. Fliesser<sup>27</sup>, G. Flügge<sup>2</sup>,  
 A. Fomenko<sup>26</sup>, J. Formánek<sup>32</sup>, J.M. Foster<sup>23</sup>, G. Franke<sup>11</sup>, E. Gabathuler<sup>20</sup>, K. Gabathuler<sup>34</sup>,  
 F. Gaede<sup>27</sup>, J. Garvey<sup>3</sup>, J. Gayler<sup>11</sup>, M. Gebauer<sup>36</sup>, H. Genzel<sup>1</sup>, R. Gerhards<sup>11</sup>, A. Glazov<sup>36</sup>,  
 L. Goerlich<sup>6</sup>, N. Gogitidze<sup>26</sup>, M. Goldberg<sup>30</sup>, D. Goldner<sup>8</sup>, K. Golec-Biernat<sup>6</sup>, B. Gonzalez-  
 Pineiro<sup>30</sup>, I. Gorelov<sup>25</sup>, C. Grab<sup>37</sup>, H. Grässler<sup>2</sup>, T. Greenshaw<sup>20</sup>, R.K. Griffiths<sup>21</sup>, G. Grindhammer<sup>27</sup>,  
 A. Gruber<sup>27</sup>, C. Gruber<sup>17</sup>, T. Hadig<sup>1</sup>, D. Haidt<sup>11</sup>, L. Hajduk<sup>6</sup>, T. Haller<sup>14</sup>, M. Hampel<sup>1</sup>,  
 W.J. Haynes<sup>5</sup>, B. Heinemann<sup>11</sup>, G. Heinzelmann<sup>13</sup>, R.C.W. Henderson<sup>19</sup>, H. Henschel<sup>36</sup>,  
 I. Herynek<sup>31</sup>, M.F. Hess<sup>27</sup>, K. Hewitt<sup>3</sup>, K.H. Hiller<sup>36</sup>, C.D. Hilton<sup>23</sup>, J. Hladký<sup>31</sup>, M. Höppner<sup>8</sup>,  
 D. Hoffmann<sup>11</sup>, T. Holtom<sup>20</sup>, R. Horisberger<sup>34</sup>, V.L. Hudgson<sup>3</sup>, M. Hütte<sup>8</sup>, M. Ibbotson<sup>23</sup>,  
 Ç. İşsever<sup>8</sup>, H. Itterbeck<sup>1</sup>, A. Jacholkowska<sup>28</sup>, C. Jacobsson<sup>22</sup>, M. Jacquet<sup>28</sup>, M. Jaffre<sup>28</sup>,  
 J. Janoth<sup>16</sup>, D.M. Jansen<sup>14</sup>, L. Jönsson<sup>22</sup>, D.P. Johnson<sup>4</sup>, H. Jung<sup>22</sup>, P.I.P. Kalmus<sup>21</sup>, M. Kander<sup>11</sup>,  
 D. Kant<sup>21</sup>, U. Kathage<sup>17</sup>, J. Katzy<sup>15</sup>, H.H. Kaufmann<sup>36</sup>, O. Kaufmann<sup>15</sup>, M. Kausch<sup>11</sup>,  
 S. Kazarian<sup>11</sup>, I.R. Kenyon<sup>3</sup>, S. Kermiche<sup>24</sup>, C. Keuker<sup>1</sup>, C. Kiesling<sup>27</sup>, M. Klein<sup>36</sup>, C. Kleinwort<sup>11</sup>,  
 G. Knies<sup>11</sup>, T. Köhler<sup>1</sup>, J.H. Köhne<sup>27</sup>, H. Kolanoski<sup>39</sup>, S.D. Kolya<sup>23</sup>, V. Korbel<sup>11</sup>, P. Kostka<sup>36</sup>,  
 S.K. Kotelnikov<sup>26</sup>, T. Krämerkämper<sup>8</sup>, M.W. Krasny<sup>6,30</sup>, H. Krehbiel<sup>11</sup>, D. Krücker<sup>27</sup>, A. Küpper<sup>35</sup>,  
 H. Küster<sup>22</sup>, M. Kuhlen<sup>27</sup>, T. Kurča<sup>36</sup>, J. Kurzhöfer<sup>8</sup>, B. Laforge<sup>9</sup>, M.P.J. Landon<sup>21</sup>, W. Lange<sup>36</sup>,  
 U. Langenegger<sup>37</sup>, A. Lebedev<sup>26</sup>, F. Lehner<sup>11</sup>, V. Lemaitre<sup>11</sup>, S. Levonian<sup>29</sup>, M. Lindstroem<sup>22</sup>,  
 F. Linsel<sup>11</sup>, J. Lipinski<sup>11</sup>, B. List<sup>11</sup>, G. Lobo<sup>28</sup>, J.W. Lomas<sup>23</sup>, G.C. Lopez<sup>12</sup>, V. Lubimov<sup>25</sup>,  
 D. Lüke<sup>8,11</sup>, L. Lytkin<sup>14</sup>, N. Magnussen<sup>35</sup>, H. Mahlke-Krüger<sup>11</sup>, E. Malinovski<sup>26</sup>, R. Maraček<sup>18</sup>,  
 P. Marage<sup>4</sup>, J. Marks<sup>15</sup>, R. Marshall<sup>23</sup>, J. Martens<sup>35</sup>, G. Martin<sup>13</sup>, R. Martin<sup>20</sup>, H.-U. Martyn<sup>1</sup>,  
 J. Martyniak<sup>6</sup>, T. Mavroidis<sup>21</sup>, S.J. Maxfield<sup>20</sup>, S.J. McMahon<sup>20</sup>, A. Mehta<sup>5</sup>, K. Meier<sup>16</sup>,  
 P. Merkel<sup>11</sup>, F. Metlica<sup>14</sup>, A. Meyer<sup>13</sup>, A. Meyer<sup>11</sup>, H. Meyer<sup>35</sup>, J. Meyer<sup>11</sup>, P.-O. Meyer<sup>2</sup>,  
 A. Migliori<sup>29</sup>, S. Mikocki<sup>6</sup>, D. Milstead<sup>20</sup>, J. Moeck<sup>27</sup>, F. Moreau<sup>29</sup>, J.V. Morris<sup>5</sup>, E. Mroczko<sup>6</sup>,  
 D. Müller<sup>38</sup>, T. Walter<sup>38</sup>, K. Müller<sup>11</sup>, P. Murín<sup>18</sup>, V. Nagovizin<sup>25</sup>, R. Nahnauer<sup>36</sup>, B. Naroska<sup>13</sup>,  
 Th. Naumann<sup>36</sup>, I. Négri<sup>24</sup>, P.R. Newman<sup>3</sup>, D. Newton<sup>19</sup>, H.K. Nguyen<sup>30</sup>, T.C. Nicholls<sup>3</sup>,  
 F. Niebergall<sup>13</sup>, C. Niebuhr<sup>11</sup>, Ch. Niedzballa<sup>1</sup>, H. Niggli<sup>37</sup>, G. Nowak<sup>6</sup>, T. Nunnemann<sup>14</sup>,  
 M. Nyberg-Werther<sup>22</sup>, H. Oberlack<sup>27</sup>, J.E. Olsson<sup>11</sup>, D. Ozerov<sup>25</sup>, P. Palmen<sup>2</sup>, E. Panaro<sup>11</sup>,  
 A. Panitch<sup>4</sup>, C. Pascaud<sup>28</sup>, S. Passaggio<sup>37</sup>, G.D. Patel<sup>20</sup>, H. Pawletta<sup>2</sup>, E. Peppel<sup>36</sup>, E. Perez<sup>9</sup>,  
 J.P. Phillips<sup>20</sup>, A. Pieuchot<sup>24</sup>, D. Pitzl<sup>37</sup>, R. Pöschl<sup>8</sup>, G. Pope<sup>7</sup>, B. Povh<sup>14</sup>, S. Prell<sup>11</sup>,  
 K. Rabbertz<sup>1</sup>, G. Rädcl<sup>11</sup>, P. Reimer<sup>31</sup>, H. Rick<sup>8</sup>, S. Riess<sup>13</sup>, E. Rizvi<sup>21</sup>, P. Robmann<sup>38</sup>,  
 R. Roosen<sup>4</sup>, K. Rosenbauer<sup>1</sup>, A. Rostovtsev<sup>30</sup>, F. Rouse<sup>7</sup>, C. Royon<sup>9</sup>, K. Rüter<sup>27</sup>, S. Rusakov<sup>26</sup>,  
 K. Rybicki<sup>6</sup>, D.P.C. Sankey<sup>5</sup>, P. Schacht<sup>27</sup>, S. Schiek<sup>13</sup>, S. Schleich<sup>16</sup>, P. Schleper<sup>15</sup>, W. von Schlippe<sup>21</sup>,  
 D. Schmidt<sup>35</sup>, G. Schmidt<sup>13</sup>, L. Schoeffel<sup>9</sup>, A. Schöning<sup>11</sup>, V. Schröder<sup>11</sup>, E. Schuhmann<sup>27</sup>,  
 B. Schwab<sup>15</sup>, F. Sefkow<sup>38</sup>, A. Semenov<sup>25</sup>, V. Shekelyan<sup>11</sup>, I. Sheviakov<sup>26</sup>, L.N. Shtarkov<sup>26</sup>,

G. Siegmon<sup>17</sup>, U. Siewert<sup>17</sup>, Y. Sirois<sup>29</sup>, I.O. Skillicorn<sup>10</sup>, T. Sloan<sup>19</sup>, P. Smirnov<sup>26</sup>, M. Smith<sup>20</sup>, V. Solochenko<sup>25</sup>, Y. Soloviev<sup>26</sup>, A. Specka<sup>29</sup>, J. Spiekermann<sup>8</sup>, S. Spielman<sup>29</sup>, H. Spitzer<sup>13</sup>, F. Squinabol<sup>28</sup>, P. Steffen<sup>11</sup>, R. Steinberg<sup>2</sup>, J. Steinhart<sup>13</sup>, B. Stella<sup>33</sup>, A. Stellberger<sup>16</sup>, J. Stier<sup>11</sup>, J. Stiewe<sup>16</sup>, U. Stößlein<sup>36</sup>, K. Stolze<sup>36</sup>, U. Straumann<sup>15</sup>, W. Struczinski<sup>2</sup>, J.P. Sutton<sup>3</sup>, S. Tapprogge<sup>16</sup>, M. Taševský<sup>32</sup>, V. Tchernyshov<sup>25</sup>, S. Tchetchelnitski<sup>25</sup>, J. Theissen<sup>2</sup>, G. Thompson<sup>21</sup>, P.D. Thompson<sup>3</sup>, N. Tobien<sup>11</sup>, R. Todenhagen<sup>14</sup>, P. Truöl<sup>38</sup>, G. Tsipolitis<sup>37</sup>, J. Turnau<sup>6</sup>, E. Tzamariudaki<sup>11</sup>, P. Uelkes<sup>2</sup>, A. Usik<sup>26</sup>, S. Valkár<sup>32</sup>, A. Valkárová<sup>32</sup>, C. Vallée<sup>24</sup>, P. Van Esch<sup>4</sup>, P. Van Mechelen<sup>4</sup>, D. Vandenplas<sup>29</sup>, Y. Vazdik<sup>26</sup>, P. Verrecchia<sup>9</sup>, G. Villet<sup>9</sup>, K. Wacker<sup>8</sup>, A. Wagener<sup>2</sup>, M. Wagener<sup>34</sup>, R. Wallny<sup>15</sup>, B. Waugh<sup>23</sup>, G. Weber<sup>13</sup>, M. Weber<sup>16</sup>, D. Wegener<sup>8</sup>, A. Wegner<sup>27</sup>, T. Wengler<sup>15</sup>, M. Werner<sup>15</sup>, L.R. West<sup>3</sup>, S. Wiesand<sup>35</sup>, T. Wilksen<sup>11</sup>, S. Willard<sup>7</sup>, M. Winde<sup>36</sup>, G.-G. Winter<sup>11</sup>, C. Wittek<sup>13</sup>, M. Wobisch<sup>2</sup>, H. Wollatz<sup>11</sup>, E. Wunsch<sup>11</sup>, J. Žáček<sup>32</sup>, D. Zarbock<sup>12</sup>, Z. Zhang<sup>28</sup>, A. Zhokin<sup>25</sup>, P. Zini<sup>30</sup>, F. Zomer<sup>28</sup>, J. Zsembery<sup>9</sup>, and M. zurNedden<sup>38</sup>.

<sup>1</sup> I. Physikalisches Institut der RWTH, Aachen, Germany<sup>a</sup>

<sup>2</sup> III. Physikalisches Institut der RWTH, Aachen, Germany<sup>a</sup>

<sup>3</sup> School of Physics and Space Research, University of Birmingham, Birmingham, UK<sup>b</sup>

<sup>4</sup> Inter-University Institute for High Energies ULB-VUB, Brussels; Universitaire Instelling Antwerpen, Wilrijk; Belgium<sup>c</sup>

<sup>5</sup> Rutherford Appleton Laboratory, Chilton, Didcot, UK<sup>b</sup>

<sup>6</sup> Institute for Nuclear Physics, Cracow, Poland<sup>d</sup>

<sup>7</sup> Physics Department and IIRPA, University of California, Davis, California, USA<sup>e</sup>

<sup>8</sup> Institut für Physik, Universität Dortmund, Dortmund, Germany<sup>a</sup>

<sup>9</sup> CEA, DSM/DAPNIA, CE-Saclay, Gif-sur-Yvette, France

<sup>10</sup> Department of Physics and Astronomy, University of Glasgow, Glasgow, UK<sup>b</sup>

<sup>11</sup> DESY, Hamburg, Germany<sup>a</sup>

<sup>12</sup> I. Institut für Experimentalphysik, Universität Hamburg, Hamburg, Germany<sup>a</sup>

<sup>13</sup> II. Institut für Experimentalphysik, Universität Hamburg, Hamburg, Germany<sup>a</sup>

<sup>14</sup> Max-Planck-Institut für Kernphysik, Heidelberg, Germany<sup>a</sup>

<sup>15</sup> Physikalisches Institut, Universität Heidelberg, Heidelberg, Germany<sup>a</sup>

<sup>16</sup> Institut für Hochenergiephysik, Universität Heidelberg, Heidelberg, Germany<sup>a</sup>

<sup>17</sup> Institut für Reine und Angewandte Kernphysik, Universität Kiel, Kiel, Germany<sup>a</sup>

<sup>18</sup> Institute of Experimental Physics, Slovak Academy of Sciences, Košice, Slovak Republic<sup>f,j</sup>

<sup>19</sup> School of Physics and Chemistry, University of Lancaster, Lancaster, UK<sup>b</sup>

<sup>20</sup> Department of Physics, University of Liverpool, Liverpool, UK<sup>b</sup>

<sup>21</sup> Queen Mary and Westfield College, London, UK<sup>b</sup>

<sup>22</sup> Physics Department, University of Lund, Lund, Sweden<sup>g</sup>

<sup>23</sup> Physics Department, University of Manchester, Manchester, UK<sup>b</sup>

<sup>24</sup> CPPM, Université d'Aix-Marseille II, IN2P3-CNRS, Marseille, France

<sup>25</sup> Institute for Theoretical and Experimental Physics, Moscow, Russia

<sup>26</sup> Lebedev Physical Institute, Moscow, Russia<sup>f</sup>

<sup>27</sup> Max-Planck-Institut für Physik, München, Germany<sup>a</sup>

<sup>28</sup> LAL, Université de Paris-Sud, IN2P3-CNRS, Orsay, France

<sup>29</sup> LPNHE, Ecole Polytechnique, IN2P3-CNRS, Palaiseau, France

<sup>30</sup> LPNHE, Universités Paris VI and VII, IN2P3-CNRS, Paris, France

<sup>31</sup> Institute of Physics, Czech Academy of Sciences, Praha, Czech Republic<sup>f,h</sup>

<sup>32</sup> Nuclear Center, Charles University, Praha, Czech Republic<sup>f,h</sup>

<sup>33</sup> INFN Roma 1 and Dipartimento di Fisica, Università Roma 3, Roma, Italy

<sup>34</sup> Paul Scherrer Institut, Villigen, Switzerland

<sup>35</sup> Fachbereich Physik, Bergische Universität Gesamthochschule Wuppertal, Wuppertal, Germany<sup>a</sup>

<sup>36</sup> DESY, Institut für Hochenergiephysik, Zeuthen, Germany<sup>a</sup>

<sup>37</sup> Institut für Teilchenphysik, ETH, Zürich, Switzerland<sup>i</sup>

<sup>38</sup> Physik-Institut der Universität Zürich, Zürich, Switzerland<sup>i</sup>

<sup>39</sup> Institut für Physik, Humboldt-Universität, Berlin, Germany<sup>a</sup>

<sup>40</sup> Rechenzentrum, Bergische Universität Gesamthochschule Wuppertal, Wuppertal, Germany<sup>a</sup>

<sup>41</sup> Visitor from Physics Dept. University Louisville, USA

<sup>a</sup> Supported by the Bundesministerium für Bildung, Wissenschaft, Forschung und Technologie, FRG, under contract numbers 6AC17P, 6AC47P, 6DO57I, 6HH17P, 6HH27I, 6HD17I, 6HD27I, 6KI17P, 6MP17I, and 6WT87P

<sup>b</sup> Supported by the UK Particle Physics and Astronomy Research Council, and formerly by the UK Science and Engineering Research Council

<sup>c</sup> Supported by FNRS-NFWO, IISN-IIKW

<sup>d</sup> Partially supported by the Polish State Committee for Scientific Research, grant no. 115/E-343/SPUB/P03/120/96

<sup>e</sup> Supported in part by USDOE grant DE F603 91ER40674

<sup>f</sup> Supported by the Deutsche Forschungsgemeinschaft

<sup>g</sup> Supported by the Swedish Natural Science Research Council

<sup>h</sup> Supported by GA ČR grant no. 202/96/0214, GA AV ČR grant no. A1010619 and GA UK grant no. 177

<sup>i</sup> Supported by the Swiss National Science Foundation

<sup>j</sup> Supported by VEGA SR grant no. 2/1325/96

# 1 Introduction

The measurement of the inclusive deep inelastic lepton-proton scattering (DIS) cross section has been of great importance for the understanding of quark and gluon substructure of the proton [1]. Recently published measurements of the structure function  $F_2$  at HERA based on analyses of the data collected in 1994 cover the range in squared four-momentum transfer  $Q^2$ , Bjorken- $x$  and inelasticity  $y$  corresponding to  $1.5 \leq Q^2 \leq 5000 \text{ GeV}^2$ ,  $3 \cdot 10^{-5} \leq x \leq 0.32$  and roughly  $y > 0.01$  [2–4]. These data have shown that  $F_2$  continues to rise strongly with decreasing  $x$  for the lowest  $Q^2$  values reached. Furthermore, it has turned out that the data can be successfully described by perturbative QCD in the measured kinematic range, using the leading twist Next to Leading Order QCD evolution equations, which have subsequently been used to extract the gluon density in the proton at low  $x$ .

The measured behaviour of  $F_2$  at low  $Q^2$  is contrary to expectations based on Regge phenomenology [5], which anticipate a much slower rise with decreasing  $x$ . At low  $x$  the center of mass energy  $W$  of the  $\gamma^*p$  system is approximately  $W \simeq \sqrt{Q^2/x}$ . Since  $F_2$  at low  $x$  is directly proportional to the total cross section of the virtual photon-proton interaction  $\sigma_{\gamma^*p}^{tot}$ , the rise of  $F_2$  with decreasing  $x$  is reflected in a strong increase of  $\sigma_{\gamma^*p}^{tot}$  with  $W$ . The rise can be quantified by parameterizing the data in the form  $F_2 \sim W^{2\lambda}$ . For low- $x$  data with  $Q^2 \geq 1.5 \text{ GeV}^2$  and  $40 < W < 200 \text{ GeV}$ , values of  $\lambda$  in the range of 0.2-0.4 have been measured [2]. This can be contrasted with the increase of the real photoproduction ( $Q^2 = 0$ ) cross section in the same range of  $W$  [6, 7] which gives a value of  $\lambda \simeq 0.08$ , similar to that observed for hadronic interactions. These processes are dominantly of non-perturbative nature and the total cross section behaviour with  $W$  is well described by Regge phenomenology which assumes that the interaction dynamics is driven by the so-called soft pomeron. The  $F_2$  data measured in the region  $Q^2 \geq 1.5 \text{ GeV}^2$  indicate that the photoproduction limit has not yet been reached. It is therefore of interest to study data at still lower  $Q^2$  values, and to experimentally establish and probe the transition between the region of perturbative QCD (DIS) and Regge phenomenology (photoproduction), a topic of much theoretical debate at present (see e.g. [8–11]).

The data presented in this paper extend the  $Q^2$  region in a continuous way down to lower values. This extension was achieved with the H1 detector at HERA by upgrading the detector components in the backward (electron<sup>1</sup> beam direction) region. A new calorimeter and a new tracking chamber with increased acceptance for small scattering angles were installed in the winter shutdown 1994/1995, and they were commissioned during the data taking period of 1995. In 1995 the incident electron energy was  $E_e = 27.5 \text{ GeV}$  and the proton energy was  $E_p = 820 \text{ GeV}$ , leading to a total center of mass energy of the collision of  $\sqrt{s} = 300 \text{ GeV}$ . The data used for this analysis result from a short data taking period where the  $ep$  collision vertex was shifted by 70 cm in the proton-beam direction with respect to the nominal vertex position to increase the acceptance for the electrons scattered through small angles. As a result the data have an acceptance in  $Q^2$  down to  $Q^2 \sim 0.3 \text{ GeV}^2$ . In this paper we present data for the kinematic range  $0.35 \leq Q^2 \leq 3.5 \text{ GeV}^2$ ,  $x \geq 6 \cdot 10^{-6}$  and  $0.03 \leq y \leq 0.75$ , and compare the results with other experiments and with Regge and QCD inspired phenomenological models.

---

<sup>1</sup>HERA operated with  $e^-p$  collisions in 1992, 1993 and the start of 1994, and  $e^+p$  collisions for the major part of 1994 and all of 1995. In this paper the incident and scattered lepton are always referred to as “electron”.

## 2 The H1 Detector

The H1 detector [12] is a nearly hermetic multi-purpose apparatus built to investigate the inelastic high-energy interactions of electrons and protons at HERA. The structure function measurement relies essentially on the tracking chamber system, the backward calorimeter and the liquid argon (LAr) calorimeter which are described briefly here.

The tracking system includes the central tracking chambers, the forward tracker modules and a backward drift chamber. These chambers are placed around the beam pipe at  $z$  positions between  $-1.5$  and  $2.5$  m. The  $+z$ -axis is in the proton beam direction. A superconducting solenoid surrounding both the tracking system and the (LAr) calorimeter provides a uniform magnetic field of  $1.15$  T.

The central jet chamber (CJC) consists of two concentric drift chambers covering a polar angle range from  $15^\circ$  to  $165^\circ$ . Polar angles are defined with respect to the  $+z$  direction. Tracks crossing the CJC are measured with a transverse momentum resolution of  $\delta p_T/p_T < 0.01 \cdot p_T$  (GeV). The CJC is supplemented by two cylindrical drift chambers at radii of  $18$  and  $47$  cm, respectively, to improve the determination of the  $z$  coordinate of the tracks. A proportional chamber is attached to each of the  $z$  drift chambers for triggering.

A tracking chamber system made of three identical modules measures charged particles emitted in the forward direction ( $7^\circ$  to  $20^\circ$ ). The forward tracker is used to determine the event vertex for the events which leave no track in the CJC. This enables vertex reconstruction of events with larger  $x$  than can be achieved with the CJC alone.

In the backward region there is an eight layer drift chamber (BDC) [13] which has a polar angle acceptance of  $151^\circ$  to  $177.5^\circ$  for collisions at the nominal vertex position. It replaces the backward multiwire proportional chamber used in previous data taking periods. For data where the vertex is shifted by  $70$  cm in the proton direction the acceptance at large angles increases to a maximum value of  $178.3^\circ$ . The BDC provides track segments for charged particles entering the backward calorimeter. These are used to identify electrons and, together with the event vertex reconstructed from tracks in the forward and central tracker, to measure their polar angle  $\theta_e$ . The resolution for reconstructed BDC hits is about  $0.5$  mm in the radial direction, and  $2.5$  mm in the azimuthal direction.

In the backward region a lead/scintillating fiber calorimeter (SPACAL) [14] was installed, replacing the previous lead/scintillator electromagnetic calorimeter (BEMC). The new calorimeter has both electromagnetic and hadronic sections. The angular acceptance of the SPACAL is  $153^\circ < \theta < 177.8^\circ$  for collisions at the nominal vertex, increasing to  $178.5^\circ$  for collisions where the interaction vertex is shifted by  $70$  cm in the proton direction. The resolution in electron energy is determined using the present data and a value of  $7.5\%/\sqrt{E(\text{GeV})} \oplus 2.5\%$  is obtained for the electromagnetic calorimeter. The absolute energy scale uncertainty is determined to be  $1\%$  at  $27.5$  GeV increasing to  $3\%$  at  $7$  GeV, which is the lowest electron energy used in this analysis. The high granularity (1192 cells) results in a spatial resolution of about  $4$  mm. Around the beam pipe the electromagnetic section of the SPACAL has a veto layer (inner and outer radius  $5.7$  cm and  $6.5$  cm respectively), which is used to detect electrons for which the shower is not fully contained laterally. The hadronic section has 128 cells. The hadronic energy scale uncertainty of the measurement in the SPACAL is presently about  $7\%$ . Both calorimeter parts have a time resolution better

than 1 ns which facilitates the reduction of proton beam induced background from beam-wall and beam-gas interactions which occur upstream of the detector.

To summarize, compared with the detector used up to the end of 1994, the upgrade of the detector components in the backward region has resulted in an increased acceptance of electrons scattered through small angles (large  $\theta_e$ ), in improved granularity and in improved resolution. When taken together with the hadronic energy measurement these features have greatly facilitated the recognition and removal of background when selecting DIS events, and have extended the available kinematic range of the measurement.

Hadronic final state energies are further measured in the LAr calorimeter [15] which covers an angular region between  $4^\circ$  and  $154^\circ$ . The calorimeter consists of an electromagnetic section with lead absorber plates and a hadronic section with stainless steel absorber plates. Both sections are highly segmented in the transverse and longitudinal directions with about 44000 cells in total. The electromagnetic part has a depth of between 20 and 30 radiation lengths. The total depth of both calorimeters varies between 4.5 and 8 interaction lengths. The hadronic energy uncertainty of the LAr calorimeter is determined to be 4%.

The luminosity is determined from the measured cross section of the Bethe Heitler (BH) reaction  $ep \rightarrow ep\gamma$ . The final state electron and photon are detected in calorimeters (electron and photon “taggers”) close to the beam pipe but at large distances from the main detector (at  $z = -33$  m and  $z = -103$  m). For the final value of the luminosity only the hard photon bremsstrahlung data are used. The precision of the luminosity determination for these data, where the interaction vertex is shifted, is 3% [16]. It results from the error on the luminosity measurement and a correction for proton “satellite” bunches in HERA which lead to collisions about 70 cm displaced with respect to the main part of the proton bunch.

### 3 Kinematics

The kinematic variables of the inclusive scattering process  $ep \rightarrow eX$  can be reconstructed in different ways using measured quantities from the hadronic final state and from the scattered electron. The choice of the reconstruction method for  $Q^2$  and  $y$  determines the size of systematic errors, acceptance and radiative corrections. The methods used in the analysis of the 1995 data are: i) the “electron method” (E), which uses only the event vertex and the reconstructed scattered electron, and which has the best resolutions in  $x$  and  $Q^2$  at large  $y$ ; ii) the “ $\Sigma$  method” ( $\Sigma$ ) [17], which uses the electron and hadronic final states measurements, which is less sensitive to radiative corrections, and which can be used from very low to large  $y$  values. Both calorimetric and track information are used to calculate the kinematics with the  $\Sigma$  method [2]. The application of different methods is an important cross check of the results.

The basic formulae for  $Q^2$  and  $y$  in the E method are:

$$y_e = 1 - \frac{E'_e}{E_e} \sin^2 \frac{\theta_e}{2} \quad Q_e^2 = 4E'_e E_e \cos^2 \frac{\theta_e}{2} = \frac{E_e'^2 \sin^2 \theta_e}{1 - y_e}, \quad (1)$$

where  $E'_e$  and  $\theta_e$  are the energy and polar angle of the scattered electron. The formulae for the  $\Sigma$  method are:

$$y_\Sigma = \frac{\Sigma}{\Sigma + E'_e(1 - \cos \theta_e)} \quad Q_\Sigma^2 = \frac{E_e'^2 \sin^2 \theta_e}{1 - y_\Sigma}, \quad (2)$$

with

$$\Sigma = \sum_h (E_h - P_{z,h}). \quad (3)$$

Here  $E_h$  and  $P_{z,h}$  are the energy and longitudinal momentum component of a particle  $h$ , the summation is over all hadronic final state particles, and masses are neglected. The denominator of  $y_\Sigma$  is equal to twice the energy of the true incident beam energy, which differs from the nominal beam energy if one or more real photons are (mostly collinearly) emitted by the incident electron and not detected. The variable  $x$  is calculated in both methods as  $x = Q^2/ys$ . The methods used are the same as those in the analysis of the 1994 data which is reported in [2].

## 4 Monte Carlo Programs and their Implementation

Acceptance corrections and background contributions are studied with the data and Monte Carlo simulations. Monte Carlo DIS events corresponding to twice the luminosity of the data were generated using DJANGO [18]. This program is based on HERACLES [19] for the electroweak interaction and on LEPTO [20] to simulate the hadronic final state. HERACLES includes complete first order radiative corrections, the simulation of real bremsstrahlung photons, and the longitudinal structure function. LEPTO uses the colour dipole model (CDM) as implemented in ARIADNE [21] which is in good agreement with data on the energy flow and other characteristics of the final state as measured by H1 [22] and ZEUS [23]. Alternatively, first order QCD matrix elements with additional parton showers can be used for the final state QCD radiation. Hadronization is performed using string fragmentation [24]. This model does not contain events with large rapidity gaps [25], tentatively interpreted as diffractive events. Such events can be generated with the Monte Carlo programs RAPGAP [26] and DIFFVM [27]. The latter generates the diffractive exclusive channels  $ep \rightarrow ep\rho^0$  and  $ep \rightarrow ep\phi$ . In the present analysis these channels to a large extent escape selection. Dedicated measurements of vector meson production cross sections have been made at HERA [28, 29], and are used to normalize the Monte Carlo prediction. The program RAPGAP generates events with a continuous mass spectrum of diffractive final states and the yield has been normalized to the rate of events with a large rapidity gap observed in the data.

The acceptance corrections were performed using in turn the GRV [30] and MRSD0' [32] parton distributions for the initial structure functions in the Monte Carlo calculations. An iterative procedure was used to reweight the input structure functions of the Monte Carlo programs with the measured  $F_2$  values in this analysis, as described in Section 6. For the figures in this paper which show a comparison of the detector response of Monte Carlo with data, the result of the final iteration of the input structure function was used.

Photoproduction background was simulated using the PHOJET [33] generator for  $\gamma p$  interactions. A sample of photoproduction events was generated which contained all classes of events (soft hadronic collisions, hard scattering processes and heavy flavour production), corresponding to three times the luminosity of the data. PHOJET was used to generate events with  $Q^2 < 0.1 \text{ GeV}^2$ , and DJANGO for events with  $Q^2 > 0.1 \text{ GeV}^2$  for acceptance and background calculations. The results reported here were found to be insensitive to the value of the  $Q^2$  boundary between the regions where the two generators were used.



The detector response of the Monte Carlo events was simulated in detail with a program based on the GEANT program [34]. After this step these events were subjected to the same reconstruction and analysis chain as the real data.

## 5 Event Selection and Calibration

The data sample used for this analysis corresponds to an integrated luminosity of  $114 \text{ nb}^{-1}$ . The trigger used requires that there be a local energy deposit (cluster) in the SPACAL calorimeter with energy greater than about 5 GeV occurring in time with an  $ep$  bunch crossing. The trigger efficiency is about 99% for electrons with an energy above 7 GeV. Losses of about 1% occur due to the event timing requirements.

Deep inelastic events are selected if they satisfy the following criteria:

- the most energetic cluster in the electromagnetic section of the SPACAL is an electron candidate (see below) with a signal within a time window of 10 ns total width around the expected value for a genuine  $ep$  collision;
- a reconstructed event vertex exists, as determined using the central or forward trackers, within 30 cm of the average event vertex position along the beam ( $z$ ) direction;
- for the electron method  $\Sigma(E_h - P_{z,h})$  is required to be larger than 35 GeV, where  $E_h$  and  $P_{z,h}$  are the energy and longitudinal momentum of a particle. The sum is over all energy deposits measured with the calorimeters.

For the electron candidate the following is required:

- the energy of the cluster must be larger than 7 GeV;
- the radius of the cluster<sup>2</sup> must be smaller than 3.5 cm;
- there must be a track segment in the BDC matched to the cluster in the SPACAL within 2 cm along the radial direction and within 2.5 cm along the azimuthal direction; the segment closest to the center of the cluster is used for the calculation of  $\theta_e$ ;
- the radial distance from the beamline to the point at which the track associated with the cluster intersects the surface of the SPACAL must be larger than 8.7 cm, corresponding roughly to an acceptance of  $\theta_e < 178^\circ$ ;
- less than 1 GeV of energy should be deposited in the veto layer of the SPACAL to avoid having too much loss of energy near the beam pipe;
- the energy measured behind the electron cluster in the hadronic part of the SPACAL, within a radius of 17.5 cm of the projected electromagnetic shower center, should be less than 0.5 GeV.

---

<sup>2</sup>The cluster radius is defined as  $\sum_i E_i * d_i / \sum_i E_i$ , where the sum is over all cluster cells;  $E_i$  is the energy of cell  $i$ , and  $d_i$  is the distance from the cluster center of gravity to the center of the cell  $i$ .

The selection cuts were designed to have a high efficiency for detecting DIS events. For a large part of the kinematic region studied the total efficiency is better than 90%.

The main non- $ep$  backgrounds in the event sample selected are due to proton beam interactions with residual gas and beam line elements upstream of the H1 detector. An efficient reduction of the background is provided by the minimum electron energy and the vertex requirements discussed above. The residual non- $ep$  background was estimated by visual inspection to be less than 2% of the total number of events at the highest  $y$ , and negligible elsewhere.

The only significant background to DIS from  $ep$  interactions is due to photoproduction events ( $Q^2 \simeq 0$ ) in which the scattered electron escapes the main detector along the beam pipe and the electron signal is faked by an energy deposition associated with the hadronic final state. For about 10% of these events the scattered electron is detected in the electron tagger, and such events can be identified as photoproduction background. The total photoproduction background was estimated from studies using simulated events from the Monte Carlo program PHOJET. The results are presented in Fig. 1, where the energy spectrum of the downstream electron tagger and the energy of the (fake) electron candidate in the SPACAL are shown for tagged photoproduction events in the data and in the Monte Carlo predictions. The Monte Carlo curves are normalized to the number of tagged events. The prediction for the remaining photoproduction background was subtracted statistically bin by bin. For each  $Q^2$  value, only the lowest  $x$  bin has a contamination larger than 5%. This contamination never exceeds 20%.

The energy scale for electrons has been determined with events at low  $y$ , for which the energy of the scattered electron is very close to the incident electron energy. The linearity of the energy response was verified with QED-Compton events for the energy range used in this analysis. The precision of the angular measurement from the BDC was estimated using tracks in the central tracker extrapolated into the BDC region. Fig. 2 shows the energy and angular distribution of electron candidates in the sample of selected DIS events, together with Monte Carlo predictions for the sum of DIS and photoproduction background in the kinematic range  $0.32 < Q^2 < 10 \text{ GeV}^2$ . The structure function of the Monte Carlo calculation is reweighted as described in Section 6. For these and following figures in this section the Monte Carlo prediction is normalized to the luminosity. Good agreement is observed between data and Monte Carlo calculations. Fig. 3 shows the distribution of  $\Sigma(E_h - P_{z,h})$  for the full data sample and for the sample with  $y > 0.55$ . The Monte Carlo calculation describes the data well. The enhancement observed around 25 GeV in Fig. 3b results from events with one or more photons collinearly emitted by the incident electron. The level to which the hadronic variables are understood is demonstrated in Fig. 4, where the distributions of the ratio of the  $y$  values measured with the  $\Sigma$  and E methods,  $y_\Sigma/y_e$ , and the transverse momentum of the hadronic system and the scattered electron,  $p_{t,h}/p_{t,e}$ , are shown. Here the data are limited to  $y_\Sigma > 0.05$  to ensure good quality reconstruction of the kinematics with the electron method, and to the region where the  $\Sigma$  method is used for the combined measurement, namely  $0.75 < Q^2 < 4.2 \text{ GeV}^2$ . In all, the detector response is well understood, allowing a precise extraction of the cross section and  $F_2$ .

## 6 Structure Function and Cross Section Measurement

The measured  $ep$  cross section in the HERA kinematic range can be expressed in terms of proton structure functions or cross sections for virtual photon-proton interactions as follows

$$\begin{aligned} \frac{d^2\sigma}{dx dQ^2} &= \frac{2\pi\alpha^2}{Q^4 x} \left(2 - 2y + \frac{y^2}{1+R}\right) F_2(x, Q^2) \\ &= \Gamma[\sigma_T(x, Q^2) + \epsilon(y)\sigma_L(x, Q^2)] \equiv \Gamma\sigma_{\gamma^*p}^{eff}(x, y, Q^2). \end{aligned} \quad (4)$$

Here  $R = F_L/(F_2 - F_L)$  where  $F_L$  is the longitudinal structure function,  $\alpha$  is the fine structure constant, and  $\sigma_L$  and  $\sigma_T$  are the cross sections for transverse and longitudinally polarized virtual photons. The flux factor,  $\Gamma$ , and the ratio of the longitudinal to the transverse flux,  $\epsilon$ , are taken to be

$$\Gamma = \frac{\alpha(2 - 2y + y^2)}{2\pi Q^2 x}, \quad \epsilon(y) = \frac{2(1 - y)}{2 - 2y + y^2}. \quad (5)$$

The quantity  $\sigma_{\gamma^*p}^{eff}$  is the effective measured virtual photon-proton cross section for  $ep$  collisions in our kinematic range, and can be determined from the data without assumptions for  $R$ . The total virtual photon-proton cross section is here defined<sup>3</sup> as

$$\sigma_{\gamma^*p}^{tot} = \sigma_T(x, Q^2) + \sigma_L(x, Q^2) \simeq \frac{4\pi^2\alpha}{Q^2} F_2(x, Q^2). \quad (6)$$

With this definition  $\sigma_{\gamma^*p}^{tot}$  depends only on  $Q^2$  and  $x$  (or  $W$ ) and the results of different experiments may easily be compared.

The virtual photon-proton cross section is determined by converting the measured number of events in a given bin into a bin averaged cross section using Monte Carlo acceptance calculations. The data are binned in a grid of  $Q^2$  and  $x$  for the region  $Q^2 > 0.75 \text{ GeV}^2$  as for previous H1 analyses, and a grid of  $Q^2$  and  $y$  for the region below  $0.75 \text{ GeV}^2$ , which optimizes the access to the smallest possible ( $Q^2, x$ ) values. Bin widths are chosen such that the number of events reconstructed in any given bin which originate from that bin is larger than 40% for the E method and larger than 30% for the  $\Sigma$  method. All detector efficiencies are determined from the data utilizing the redundancy of the apparatus. Apart from small extra corrections, all efficiencies are correctly reproduced by the Monte Carlo simulation, and therefore the Monte Carlo can safely be used to correct for acceptance and efficiency effects. The bin averaged cross section is corrected for first order QED radiative contributions with the program HERACLES. The effective virtual photon-proton cross section,  $\sigma_{\gamma^*p}^{eff}$ , is finally obtained by correcting the bin averaged cross sections for each bin to the values at the given bin centers.

To extract the structure function  $F_2$  from these measurements an assumption has to be made for the longitudinal structure function  $F_L$  since it has not yet been measured in this kinematic region. In this analysis the model of [37] is applied for the calculation of  $R$ . These values of  $R$  are then used to determine the  $F_2$  values, as well as to reweight Monte Carlo events. The model is based on the photon-gluon fusion process and has the proper limit

<sup>3</sup>The exact formula used is  $\sigma_{\gamma^*p}^{tot} = (4\pi^2\alpha/Q^4)(4M^2x^2 + Q^2)/(1-x) \cdot F_2(x, Q^2)$  [35, 36], which is approximately equal to eqn. 6 in the HERA kinematic range;  $M$  is the proton mass.

for  $Q^2 \rightarrow 0$  where  $F_L$  should vanish  $\propto Q^4$ . The predictions of this model for the values of  $R$  in our kinematic region vary from 0.1 at  $Q^2 = 0.35 \text{ GeV}^2$  to 0.3 at  $Q^2 = 3.5 \text{ GeV}^2$ . The predictions for  $R$  at higher  $Q^2$  are in agreement with measurements from fixed target experiments. It should be noted that this is a model and future measurements could reveal quite different  $R$  values. However, only the lowest  $x$  point at each  $Q^2$  is affected significantly by the assumption made for  $R$ . If  $R$  is taken to be zero rather than the values obtained using the above model, the variation in  $F_2$  is 5 to 10% at the highest  $y$  (smallest  $x$ ) at a given  $Q^2$ , and smaller elsewhere.

Values of  $F_2$  are derived using an iterative procedure. An initial determination of the  $F_2$  values uses a structure function parameterization in the Monte Carlo simulation as described in Section 3 and it assumes a value for  $R$  as given above. A new structure function for the full range in  $Q^2$  is then calculated following the prescription of Badelek and Kwiecinski (BK, [38]), where the structure function is assumed to be the sum of two contributions: a Vector Meson Dominance (VMD) model term  $F_2^{VMD}$  and a partonic term  $F_2^{part}$ . The latter becomes dominant above  $Q^2 \sim 1 \text{ GeV}^2$ . In this analysis the result of a QCD fit similar to that reported in [2] is used for the partonic term. This fit was made to structure function data from H1 [2], and in order to constrain the high- $x$  region, to NMC [39] and BCDMS [40] data. Parton density parameterizations were defined at a starting scale  $Q_0^2 = 0.35 \text{ GeV}^2$ , and data with  $Q^2 > 1 \text{ GeV}^2$  were fitted, yielding values for  $F_2$  denoted as  $F_2^{H1QCD}$  in the following. The newly measured low  $Q^2$  data points and the measurements at  $Q^2 = 0$  in the  $W$  range at HERA [6, 7] were fitted to the form

$$F_2(x, Q^2) = C_{VM} F_2^{VMD}(x, Q^2) + \frac{Q^2}{Q^2 + Q_{VM}^2} F_2^{H1QCD}(\bar{x}, Q^2 + Q_{VM}^2), \quad (7)$$

with  $\bar{x} = (Q^2 + Q_{VM}^2)/(W^2 + Q^2 + Q_{VM}^2)$ . The fit parameters are the meson mass cut-off parameter  $Q_{VM}^2$  and the normalization of the vector meson term  $C_{VM}$ . The latter parameter is not part of the BK model and was introduced to reproduce the real photoproduction data measured at HERA in a phenomenological way. Values of  $Q_{VM}^2 = 0.45 \text{ GeV}^2$  and  $C_{VM} = 0.77$  are obtained<sup>4</sup>. It was checked that no further iteration step was needed. The Monte Carlo curves discussed in Section 4 are reweighted with these  $F_2$  values (and the  $R$  values discussed above).

A list of sources of systematic errors in the  $F_2$  determination is given below.

- Uncertainty of the electron energy scale in the SPACAL, varying from 1% at large electron energies to 3% at 7 GeV.
- A 4% scale error for the hadronic energy in the LAr calorimeter, the effect of which is reduced due to the joint consideration of tracks and calorimeter cells for the  $\Sigma$  analysis. A 7% scale error was assigned to the energy of the hadronic final state measured in the SPACAL.
- A potential shift of up to 0.5 mrad for the electron polar angle.
- For the electron identification efficiency the error was taken to be 30% of the fraction of events lost by the cuts, as given by the DIS Monte Carlo.

---

<sup>4</sup>Note that this procedure does not guarantee a consistent separation of  $F_2$  into the  $F_2^{VMD}$  and  $F_2^{part}$  contributions, as prescribed by the model.

$Q^2$ (GeV <sup>2</sup> )	$x$	$y$	$W$ (GeV)	$\kappa\sigma_{\gamma^*p}^{eff}$	$R$	$F_2$	$\delta_{stat}$ (%)	$\delta_{syst}$ (%)	$\delta_{tot}$ (%)
0.35	0.0000061	0.640	240.	0.384	0.10	0.397	5.5	14.5	15.5
0.50	0.0000086	0.640	240.	0.473	0.13	0.494	3.6	11.1	11.7
0.65	0.0000112	0.640	240.	0.539	0.16	0.568	3.6	10.4	11.0
0.65	0.0000164	0.440	199.	0.536	0.15	0.547	2.9	8.8	9.2
0.85	0.0000138	0.682	248.	0.664	0.19	0.713	5.0	13.0	13.9
0.85	0.000020	0.470	206.	0.628	0.19	0.646	2.6	6.6	7.1
0.85	0.000032	0.294	163.	0.615	0.18	0.621	2.4	7.2	7.6
0.85	0.000050	0.188	130.	0.576	0.18	0.578	2.8	8.1	8.6
0.85	0.000080	0.118	103.	0.533	0.17	0.534	3.1	15.4	15.7
1.20	0.000020	0.664	245.	0.793	0.23	0.857	3.5	10.5	11.0
1.20	0.000032	0.415	194.	0.741	0.22	0.759	2.6	7.1	7.6
1.20	0.000050	0.266	155.	0.709	0.22	0.715	2.2	6.9	7.2
1.20	0.000080	0.166	122.	0.626	0.21	0.627	2.1	8.9	9.2
1.20	0.000130	0.102	96.	0.569	0.21	0.570	2.4	5.1	5.6
1.20	0.000200	0.066	77.	0.525	0.21	0.525	2.4	5.2	5.8
1.20	0.000320	0.042	61.	0.531	0.21	0.531	2.4	7.9	8.3
1.50	0.000032	0.519	217.	0.817	0.25	0.855	3.2	8.8	9.4
1.50	0.000050	0.332	173.	0.771	0.25	0.783	2.7	5.9	6.4
1.50	0.000080	0.208	137.	0.687	0.24	0.690	2.4	6.9	7.3
1.50	0.000130	0.128	107.	0.668	0.23	0.669	2.5	6.6	7.1
1.50	0.000200	0.083	87.	0.645	0.23	0.645	2.5	7.4	7.8
1.50	0.000320	0.052	68.	0.613	0.23	0.613	2.5	6.9	7.4
1.50	0.000500	0.033	55.	0.577	0.23	0.577	2.5	7.9	8.3
2.00	0.000032	0.692	250.	0.945	0.29	1.048	5.0	12.9	13.9
2.00	0.000050	0.443	200.	0.908	0.28	0.939	3.2	6.0	6.8
2.00	0.000080	0.277	158.	0.743	0.27	0.751	2.9	5.8	6.5
2.00	0.000130	0.170	124.	0.727	0.26	0.729	2.7	7.6	8.0
2.00	0.000200	0.111	100.	0.716	0.26	0.717	2.8	5.8	6.4
2.00	0.000320	0.069	79.	0.727	0.25	0.727	2.8	5.9	6.6
2.00	0.000500	0.044	63.	0.639	0.25	0.639	2.9	8.3	8.8
2.50	0.000050	0.554	224.	0.973	0.30	1.034	4.3	11.2	12.0
2.50	0.000080	0.346	177.	0.932	0.29	0.950	3.3	5.4	6.3
2.50	0.000130	0.213	139.	0.917	0.28	0.922	2.9	7.6	8.1
2.50	0.000200	0.138	112.	0.840	0.27	0.842	2.8	6.8	7.4
2.50	0.000320	0.086	88.	0.702	0.27	0.703	3.1	5.3	6.1
2.50	0.000500	0.055	71.	0.649	0.26	0.649	3.2	6.8	7.6
2.50	0.000800	0.035	56.	0.590	0.26	0.590	3.3	8.2	8.9
3.50	0.000080	0.484	209.	1.045	0.32	1.094	4.1	8.6	9.5
3.50	0.000130	0.298	164.	1.003	0.31	1.018	3.5	5.0	6.1
3.50	0.000200	0.194	132.	0.869	0.30	0.873	3.3	7.2	7.9
3.50	0.000320	0.121	105.	0.898	0.29	0.899	3.2	8.5	9.1
3.50	0.000500	0.077	84.	0.863	0.28	0.864	3.4	6.5	7.3
3.50	0.000800	0.048	66.	0.686	0.28	0.686	3.6	7.4	8.2
3.50	0.001300	0.030	52.	0.663	0.27	0.663	3.6	7.5	8.3

Table 1: Proton structure function  $F_2(x, Q^2)$  and effective virtual photon-proton cross section  $\sigma_{\gamma^*p}^{eff}(W, Q^2)$ , scaled by the kinematic factor  $\kappa = Q^2/(4\pi^2\alpha)$ , with statistical ( $\delta_{stat}$ ), systematic ( $\delta_{syst}$ ) and total ( $\delta_{tot}$ ) fractional errors. The normalization uncertainty, not included in the systematic error, is 3%. The values of  $R$  used to calculate  $F_2$  are also given.

- The following contributions to the systematic errors from the event selection were included: trigger and timing veto 0.5%; BDC efficiency 2%; vertex finding efficiency 2%. For the region  $y < 0.05$  the systematic error on the vertex finding efficiency was increased to 5%.
- For the radiative corrections an error of 2% is taken everywhere, except for the highest  $y$  point of each  $Q^2$  bin and for all points with  $Q^2 \leq 0.65 \text{ GeV}^2$ , where it is increased to 5% for the electron method. This error is due to uncertainties in the hadronic corrections, in the cross section extrapolation towards  $Q^2 = 0$ , in the higher order corrections and the absence of soft photon exponentiation in the HERACLES Monte Carlo. These effects were studied using the program HECTOR [41].
- The uncertainty due to photoproduction background was assumed to be 30% of the correction applied, i.e. smaller than 6%. This affects only the highest  $y$  bins at low  $Q^2$ .
- An additional error of 3% was assigned to the measurements using the  $\Sigma$  method to allow for the uncertainties in the hadronic final state simulation of the Monte Carlo programs. This error was determined by comparing the results of different reconstruction methods for the hadronic final state, using the combined information of calorimeter cells and tracks, or by using calorimeter cells only.
- The effect of reduced efficiency for detecting diffractive events, such as the exclusive channel  $ep \rightarrow ep\rho^0$ , has been estimated using the Monte Carlo programs for diffractive processes discussed in Section 4. Cross section corrections of up to 6% are applied for the points at the highest  $y$  values, and half of the correction was added to the systematic error. The effect is largest at the highest  $y$  values where the decay products of the meson often escape detection in the CJC and FT, and hence no event vertex is found.
- The overall normalization uncertainty is 3% due to the uncertainty in the luminosity determination.

These systematic uncertainties affect differently the  $F_2$  measurements made with different methods. In Fig. 5 the comparison of the measurements made with the E and with the  $\Sigma$  method is shown. The statistical and systematic errors are added in quadrature. The agreement between the two data sets is very good.

For the final result the values obtained with the E method are taken<sup>5</sup>, supplemented with  $\Sigma$  points at low  $y$  ( $0.03 < y < 0.12$ ) where no points from the E method are available. The result is shown in Fig. 6 and tabulated in Table 1. Both  $F_2$  and  $\sigma_{\gamma^*p}^{eff}$  are given. The latter has been multiplied by  $Q^2/(4\pi^2\alpha)$  to demonstrate directly the effect of  $R$ . The table also contains the statistical, systematic and total errors and the value of  $R$  used for the  $F_2$  calculation. A table delineating the many different correlated and uncorrelated error contributions is available on request to the H1 collaboration. The measurements have a typical systematic error of 5-10%. Compared with the previous H1 analysis [2] the  $F_2$  measurement has been extended to lower  $Q^2$  (from  $1.5 \text{ GeV}^2$  to  $0.35 \text{ GeV}^2$ ), and to lower  $x$  (from  $3 \cdot 10^{-5}$  to  $6 \cdot 10^{-6}$ ).

---

<sup>5</sup>This procedure is used except for the highest  $x$  point at  $Q^2 = 1.5 \text{ GeV}^2$ . For this point the total error calculated with the  $\Sigma$  method is almost a factor of two better than that of the E method, and therefore the  $\Sigma$  method is used.

## 7 Discussion of the Results

In Fig. 7 the  $F_2$  data are compared with previous H1 measurements [2], with the fixed target measurements of E665 [42] and NMC [39], and with the predictions of models for  $F_2$  at low  $x$ . In the region of overlap the results are in good agreement with our previous measurements and the total error has been reduced by a factor of 2 to 3. The data also show a smooth continuation from the fixed target measurements towards the low- $x$  region at HERA. The rise of  $F_2$  with decreasing  $x$  is still clearly prominent for values of  $Q^2 \geq 2 \text{ GeV}^2$  but becomes less steep for smaller  $Q^2$  values.

In Fig. 8, values of  $\lambda$  are shown from fits of the form  $F_2 \propto x^{-\lambda}$  ( $\sim W^{2\lambda}$ ) at fixed  $Q^2$  to the present H1  $F_2$  data. For each  $Q^2$  bin with  $Q^2 \geq 0.85 \text{ GeV}^2$  and  $x < 0.1$  the exponent  $\lambda$  was determined taking into account the point to point systematic error correlations. Note that this is merely a convenient parameterization to show the change of the slope with various  $Q^2$  in a quantitative way. Due to the HERA kinematics the  $x$  region in which the data are fitted is different for the  $Q^2$  values used. The result is given in Table 2. Fig. 8 also includes the H1 measurements of  $\lambda$  reported in [2]. The newly measured values are consistent with the previous low- $Q^2$  measurements, and are in the range  $\sim 0.1 - 0.2$ .

$Q^2$ (GeV <sup>2</sup> )	$\lambda$	$\delta\lambda_{stat}$	$\delta\lambda_{syst}$
0.85	0.146	0.033	0.101
1.2	0.192	0.018	0.038
1.5	0.128	0.019	0.036
2.0	0.133	0.022	0.038
2.5	0.216	0.020	0.043
3.5	0.172	0.021	0.031

Table 2: *The values of the exponent  $\lambda$  as a function of  $Q^2$ , together with the statistical ( $\delta\lambda_{stat}$ ) and systematic ( $\delta\lambda_{syst}$ ) contribution to the error.*

Fig. 9 shows  $\sigma_{\gamma^*p}^{tot}$  as a function of the  $\gamma^*p$  center of mass energy  $W$  for fixed values of  $Q^2$ . The H1 data are compared with low energy measurements and with photoproduction data. The low energy measurements are at slightly different  $Q^2$  values and were propagated to the values indicated on the figure using the ALLM parameterization [43] (see below).

In Fig. 10  $\sigma_{\gamma^*p}^{eff}$  is shown as a function of  $Q^2$  for  $W$  values above 60 GeV. The data are transformed to the  $W$  values given using the ALLM parameterization. The new results presented in this analysis help to close the gap between measurements of real and virtual photoproduction and provide further information on the transition between real and virtual photon interactions.

Several phenomenological parameterizations based on models have been proposed to describe the region at low  $Q^2$  and the transition from photoproduction to DIS, often using ingredients both from Regge theory at low  $Q^2$ , and from QCD when  $Q^2$  is of the order of 1 GeV<sup>2</sup> or larger (for a recent review, see e.g. [9]). A smooth transition from the photoproduction to the DIS regime is generally assumed, but there is still uncertainty as to how this transition takes place and as to the underlying dynamics.

Parameterizations motivated by Regge theory relate the structure function to Reggeon and pomeron exchange phenomena which successfully describe the slow rise of the total cross section with the center of mass system energy in hadron-hadron and real photon-proton interactions. The model of Donnachie and Landshoff [5] (DOLA) assumes a pomeron intercept of  $1 + \lambda \sim 1.08$  for the energy dependence of the cross section, independent of the virtuality of the photon. Fig. 7 shows that the model gives, as expected from the  $\lambda$  measurements as a function of  $Q^2$ , a prediction of  $F_2$  which is too low for the region of  $Q^2 \geq 0.85 \text{ GeV}^2$ , but which approaches the data for the lowest  $Q^2$  values. The DOLA prediction can also be interpreted as the contribution of soft pomeron exchange to the cross section at non-zero  $Q^2$ .

In the approach of Capella et al. [10] (CKMT) it is assumed that screening corrections and multi-pomeron exchange contribute less with increasing  $Q^2$ , leading to a  $Q^2$  dependent power  $\lambda$ . Hence, the structure function  $F_2$  predicted by CKMT rises faster with decreasing  $x$  for increasing  $Q^2$  than the DOLA calculations. Furthermore, the model assumes that this prescription accounts for non-perturbative contributions to  $F_2$  at a  $Q_0^2$  scale of about  $2 \text{ GeV}^2$ , from where, at higher  $Q^2$ , perturbative QCD (pQCD) evolution equations are applied to predict the  $Q^2$  dependence of  $F_2$ . As expected, Fig. 7 shows that the prediction<sup>6</sup> is systematically above that from DOLA, but it is still below the data for all but the lowest values of  $Q^2$ .

The parameterization of Abramowicz et al. [43] (ALLM) assumes that the total  $\gamma^*p$  cross section consists of two contributions which distinguish Reggeon and pomeron exchange and the behaviour of the power  $\lambda$  is assumed to vary with  $Q^2$  in a logarithmic way, emulating pQCD evolution in the high  $Q^2$  region. In Fig. 9 it is shown that the prediction is below the data for small  $Q^2$  values, but agrees with the data for  $Q^2 > 2 \text{ GeV}^2$ .

Contrary to these Regge inspired models, the model of Glück, Reya and Vogt [30] (GRV) is defined completely within the parton picture. It is assumed that all parton distributions at very low  $Q_0^2 = 0.34 \text{ GeV}^2$  have a valence-like shape, i.e. vanish for  $x \rightarrow 0$ . Assuming further that  $F_2$  evolves towards large  $Q^2$  values via parton radiation which is given by the leading twist QCD evolution equations, GRV predict that the structure function  $F_2$  should rise with decreasing  $x$ , even for low values of  $Q^2 \sim 1 \text{ GeV}^2$ . Fig. 7 shows that the GRV distributions describe the data well for  $Q^2 \geq 1 \text{ GeV}^2$ , but are systematically lower than the data for  $Q^2 < 1 \text{ GeV}^2$ . At low  $Q^2$  values the QCD evolution is over a range of  $Q^2$  which is too small, and the parton distributions become dominated by the valence behaviour at the starting scale  $Q_0^2$ .

The model of Badelek and Kwiecinski [38] (BK) combines the concepts of Vector Meson Dominance (VMD) with dynamical parton models such as that of GRV. It has per force a smooth transition from pQCD to the real photon limit, which coincides with the region measured here. The BK model predicts the  $F_2$  values very well as shown in Fig. 7. In Fig. 9 BK is compared with the total  $\gamma^*p$  cross section measurement and also shows good agreement.

A different approach to the low  $Q^2$  behaviour of  $F_2$  in the transition region between photoproduction and DIS has been presented in [11] by Adel, Barreiro and Yndurain (ABY). It assumes that perturbative QCD evolution is applicable to the lowest values of  $Q^2$ . In addition to the flat or so called “soft” behaviour of  $F_2$  with decreasing  $x$  for  $Q^2 \sim 1 \text{ GeV}^2$ ,

---

<sup>6</sup> The CKMT curves shown in Fig. 7 were calculated using the parameters given in [10] without QCD evolution. Therefore the prediction is not shown for the highest  $Q^2$  value.



which is manifest in for example the GRV model, a “harder” contribution is introduced to prevent  $F_2$  decreasing with decreasing  $x$  for  $Q^2$  values below 1 GeV<sup>2</sup>. In [11] the prescription for this contribution is singular  $\sim x^{-\lambda_s}$ , with  $\lambda_s = 0.48$  independent of  $Q^2$ . Furthermore the strong coupling constant is assumed to become independent of  $Q^2$  for values below roughly 1 GeV<sup>2</sup>, that is  $\alpha_s$  “saturates”. The result of a fit of the ABY approach to data, reported in [11], is compared with the new  $F_2$  results presented here in Fig. 7. There is good agreement at low  $x$ , but also some possible disagreement in the higher  $(x, Q^2)$  region shown in the figure. Fig. 7 also shows that in this prescription, at low  $Q^2$ , the rise of  $F_2$  with decreasing  $x$  occurs at lower  $x$  compared to the other approaches, namely for  $x < 10^{-4}$ .

In Fig. 10, BK and ALLM are compared with the measurements of  $\sigma_{\gamma^*p}^{eff}$ . To ensure consistency, for the BK prediction the value of  $R$  has been taken from [37]. The ALLM prediction as calculated here is for  $R = 0$  and therefore it is not shown for the largest  $W$ . For the other values of  $W$  the effect of  $R$  is a few percent. The measurements suggest that in the current ALLM parameterization the transition towards photoproduction behaviour occurs at too large a  $Q^2$ , in contrast to the BK approach. However BK predict a photoproduction cross section which is larger than the measurements, as shown in the figure. Fig. 10 also shows the H1 fit based on BK, as discussed in Section 6. The photoproduction cross section measurements at HERA were used in the fit, which leads to a stronger turn-over to the photoproduction regime compared to the original BK model. This fit gives a good phenomenological description of all data shown in the figure.

In summary, it turns out that the region  $0.1 < Q^2 < 1$  GeV<sup>2</sup> spans the kinematic range in which Regge or VMD inspired models describe the data at low  $Q^2$ , and models based on pQCD account well for the higher  $Q^2$  domain. Although in general several of these models show the correct qualitative behaviour of the data, none of them gives at present a completely satisfactory description of the data. Future studies will have to show if this can be remedied by adjusting the parameterizations whilst simultaneously preserving their internal consistency. The data in the low  $(x, Q^2)$  region will help to discriminate between different theoretical approaches to low- $Q^2$  dynamics.

Finally a parameterization is given of H1 data in the region  $0.35 \leq Q^2 \leq 5000$  GeV<sup>2</sup> and  $y \geq 0.01$ . Starting from the double asymptotic expression for  $F_2$  as developed in [44], a QCD inspired parameterization with only two parameters was reported in [45]. Here,  $F_2$  is parameterized as

$$F_2 = N_f x^{-\gamma} \sqrt{T/\ln(1/x)} \quad (8)$$

with  $T = \ln[\ln((Q^2 + Q_0^2)/\Lambda_{eff}^2)/\ln(Q_0^2/\Lambda_{eff}^2)]$  and  $N_f = 5n_f\sqrt{\gamma/\pi}/324$ , where  $n_f$  is the number of quark flavours, taken to be equal to four. The parameter  $\Lambda_{eff}$  resembles the QCD mass scale. The function  $T$  has been slightly changed with respect to the original proposal [45] so as to achieve a smooth behaviour over the whole  $Q^2$  range. The parameter  $\gamma$  is defined as  $\sqrt{12/(11 - 2n_f/3)}$ . Fitting this expression to the H1 data gives  $Q_0^2 = 373 \pm 24$  (*stat.*)  $\pm 42$  (*syst.*) MeV<sup>2</sup> and  $\Lambda_{eff} = 247 \pm 11$  (*stat.*)  $\pm 19$  (*syst.*) MeV, with a  $\chi^2/ndf = 156/231$  (full errors). Although eqn. 8 does not satisfy the constraint, imposed by current conservation, that  $F_2$  should vanish at  $Q^2 = 0$ , it constitutes a compact QCD-inspired parameterization of all H1 measurements of  $F_2$ .

## 8 Summary

A measurement has been presented of the proton structure function  $F_2(x, Q^2)$  and virtual photon-proton cross section  $\sigma_{\gamma^*p}^{eff}(x, y, Q^2)$  in deep inelastic electron-proton scattering at low  $Q^2$  with data taken in the 1995 HERA running period. These are the first measurements made with the upgraded backward calorimeter and drift chamber of the H1 detector.

The measurements presented are obtained using two different methods to reconstruct the inclusive scattering kinematics, allowing both a powerful internal cross check of the data and the measurement in a large kinematic region. The data cover the region of  $Q^2$  between 0.35 GeV<sup>2</sup> and 3.5 GeV<sup>2</sup> and with Bjorken- $x$  values down to  $6 \cdot 10^{-6}$ . The measurements show a smooth transition from the fixed target high- $x$  data to the HERA low- $x$  data.

The distinct rise of the structure function with decreasing  $x$  in the low- $x$  region, which is very prominent for  $Q^2 \geq 2$  GeV<sup>2</sup>, diminishes at lower  $Q^2$  values. When taken together with the data from fixed target experiments, the rise observed for the smallest  $Q^2$  values approaches that expected in Regge and VMD interpretations.

The data have been compared with different models which aim to describe the whole  $Q^2$  region. Several of these models predict the correct qualitative behaviour observed in the data but presently do not agree with the data throughout the full kinematic range. The data access the transition region from DIS to photoproduction and provide powerful constraints on the development of further low- $Q^2$  phenomenology.

### Acknowledgements

We are very grateful to the HERA machine group whose outstanding efforts made this experiment possible. We acknowledge the support of the DESY technical staff. We appreciate the substantial effort of the engineers and technicians who constructed and maintain the detector. We thank the funding agencies for financial support of this experiment. We wish to thank the DESY directorate for the support and hospitality extended to the non-DESY members of the collaboration. We are grateful to B. Badelek and A. Vogt for providing us with the calculations of  $R$  (BK) and  $F_2$  (GRV), respectively, in the region of our data.

### References

- [1] for recent reviews see:  
R. Ball and A. De Roeck, Proceedings of the Workshop on Deep Inelastic Scattering, Rome 1996, Eds. A. Negri and G. D'Agostini, in litt., and DESY preprint 96-185;  
H. Abramowicz, Proceedings of the International Conference on High Energy Physics, Warsaw 1996, Eds. A. Wroblewski, in litt., and Tel-Aviv preprint TAUP-2396-96.
- [2] H1 Collab., S. Aid et al., Nucl. Phys. **B470** (1996) 3.
- [3] ZEUS Collab., M. Derrick et al., Z. Phys. **C72** (1996) 399.
- [4] H1 Collab., C. Adloff et al., DESY preprint 96-236 (1996).

- [5] A. Donnachie and P. V. Landshoff, *Z. Phys.* **C61** (1994) 139.
- [6] H1 Collab., T. Aid et al., *Z. Phys.* **C69** (1995) 27.
- [7] ZEUS Collab., M. Derrick et al, *Z. Phys.* **C63** (1994) 408.
- [8] B. Badelek, J. Kwiecinski, *Rev. Mod. Phys.* **68** (1996) 445.
- [9] A. Levy, Proceedings of the Workshop on Deep Inelastic Scattering, Rome 1996, Eds. A. Negri and G. D'Agostini, and Tel-Aviv preprint TAUP-2349-96 (1996);  
A. Levy, DESY preprint DESY 97-013 (1997).
- [10] A. Capella et al., *Phys. Lett.* **B337** (1994) 358.
- [11] K. Adel, F. Barreiro and F.J. Yndurain, FTUAM preprint 96-39 (1996).
- [12] H1 Collab., I. Abt et al., *Nucl. Instr. and Meth.* **A386** (1997) 310 and **A386** (1997) 348.
- [13] H1 Collab., Technical Proposal for the Upgrade of the Backward Region of the H1 Detector, DESY internal report PRC-93/02.
- [14] H1 SPACAL group, R.D. Appuhn et al., DESY preprint 96-171, submitted to *Nucl. Instr. and Meth.*
- [15] H1 Calorimeter Group, B. Andrieu et al., *Nucl. Instr. and Meth.* **A336** (1993) 460.
- [16] H1 Collab.: "Luminosity Measurement in the H1 Experiment at HERA", contributed paper to the International Conference on High Energy Physics, Warsaw 1996, ICHEP96-pa17-026.
- [17] U. Bassler and G. Bernardi, *Nucl. Instr. and Meth.* **A361** (1995) 197.
- [18] G. A. Schuler and H. Spiesberger, Proceedings of the Workshop Physics at HERA, vol. 3, Eds. W. Buchmüller and G. Ingelman, DESY (1992) 1419.
- [19] A. Kwiatkowski, H. Spiesberger and H.-J. Möhring, *Comp. Phys. Comm.* **69** (1992) 155.
- [20] G. Ingelman, Proceedings of the Workshop Physics at HERA, vol. 3, Eds. W. Buchmüller and G. Ingelman, DESY (1992) 1366.
- [21] L. Lönnblad, *Comp. Phys. Comm.* **71** (1992) 15.
- [22] H1 Collab., I. Abt et al., *Z. Phys.* **C63** (1994) 377.
- [23] ZEUS Collab., M. Derrick et al., *Z. Phys.* **C59** (1993) 231.
- [24] T.Sjöstrand and M.Bengtsson, *Comp. Phys. Comm.* **43** (1987) 367;  
H.-U.Bengtsson and T.Sjöstrand, *Comp. Phys. Comm.* **46** (1987) 43;  
T.Sjöstrand, CERN-TH-6488 (1992).
- [25] ZEUS Collab., M. Derrick et al., *Phys. Lett.* **B315** (1993) 481;  
H1 Collab., T.Ahmed et al., *Nucl. Phys.* **B429** (1994) 477.
- [26] H. Jung, *Comp. Phys. Comm.* **86** (1995) 147.
- [27] B. List, Diplome Thesis, Technical University of Berlin (1993) (unpublished).

- [28] H1 Collab., S. Aid et al., Nucl. Phys. **B468** (1996) 3;  
H1 Collab., S. Aid et al., Nucl. Phys. **B463** (1996) 3.
- [29] ZEUS Collab., M. Derrick et al., Z. Phys. **C69** (1995) 39;  
ZEUS Collab., M. Derrick et al, Phys. Lett. **B380** (1996) 220;  
ZEUS Collab., M. Derrick et al, Z. Phys. **C69** (1995) 39.
- [30] M. Glück, E. Reya and A. Vogt, Z. Phys. **C67** (1995) 433;  
We show the parameterizations as presented in:  
A. Vogt, Proceedings of the Workshop on Deep-Inelastic Scattering and QCD, Paris (1995) 261, using the NLO charm contribution as calculated in [31].
- [31] E. Laenen et al., Nucl. Phys. **B392** (1993) 162, *ibid.* (1993) 229;  
E. Laenen et al., Phys. Lett. **B291** (1992) 325;  
S. Riemersma et al., Phys. Lett. **B347** (1995) 143.
- [32] A.D Martin, W.J. Stirling and R.G. Roberts, Phys. Lett. **B306** (1993) 145; **B309** (1993) 492.
- [33] R. Engel and J. Ranft, Phys. Rev. **D54** (1996) 4244.
- [34] R. Brun et al., GEANT3 User's Guide, CERN-DD/EE 84-1, Geneva (1987).
- [35] L.N. Hand, Phys. Rev. **129** (1963) 1834.
- [36] A. Levy and U. Maor, Phys. Lett. **B182** (1984) 108.
- [37] B. Badelek, J. Kwiecinski and A. Stasto, Durham preprint DTP/96/16 (1996).
- [38] B. Badelek and J. Kwiecinski, Phys. Lett. **B295** (1992) 263.
- [39] NMC Collab., M. Arneodo et al., Phys. Lett. **B364** (1995) 107;  
NMC Collab., M. Arneodo et al., hep-ph/9610231 preprint, (1996).
- [40] BCDMS Collab., A.C. Benvenuti et al., Phys. Lett. **B223** (1989) 485;  
CERN preprint CERN-EP/89-06.
- [41] A. Arbuzov et al., Comp. Phys. Comm. **94** (1996) 128.
- [42] E665 Collab., M.R. Adams et al., Phys. Rev. **D54** (1996) 3006.
- [43] H. Abramowicz, E.M. Levin, A. Levy and U. Maor, Phys. Lett. **B269** (1991) 465;  
We show the parameterizations as presented in:  
A. Marcus MSc. thesis Tel-Aviv University TAUP 2350-96 (1996) (unpublished).
- [44] R.D. Ball, S. Forte, Phys. Lett. **B335** (1994) 77;  
R.D. Ball and S. Forte, "XXXV Cracow School of Theoretical Physics", Zakopane, 1995,  
Acta Phys. Pol. **B26** (1995) 2097.
- [45] A. De Roeck, M. Klein and T. Naumann, Phys. Lett. **B385** (1996) 411.

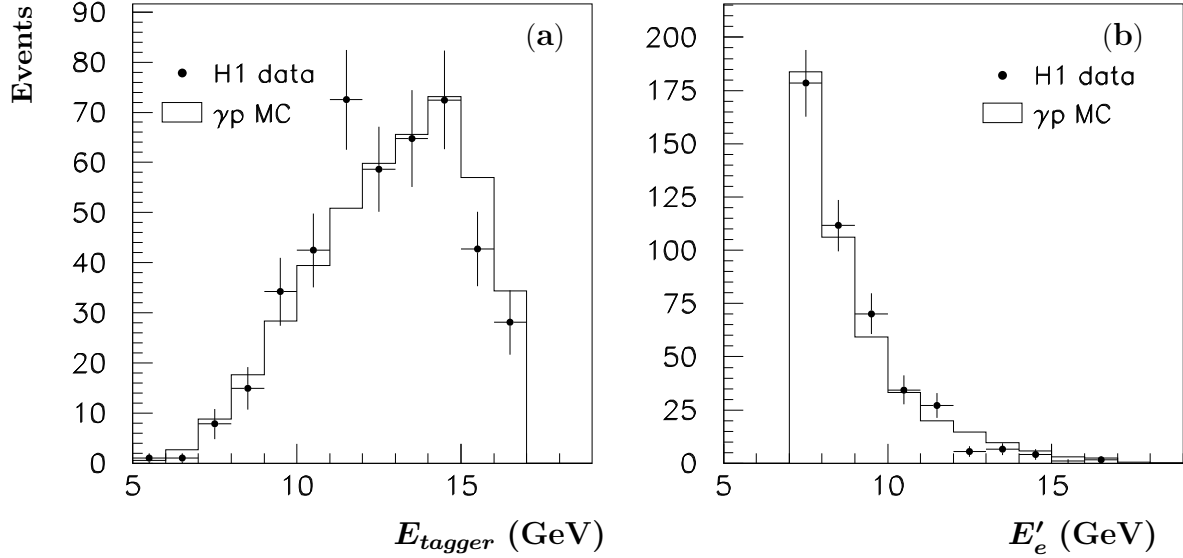


Figure 1: *Experimental (points) and Monte Carlo (solid lines) distributions of a) the energy in the electron tagger, and b) the energy of the (fake) electron candidate in the SPACAL, for tagged photoproduction events.*

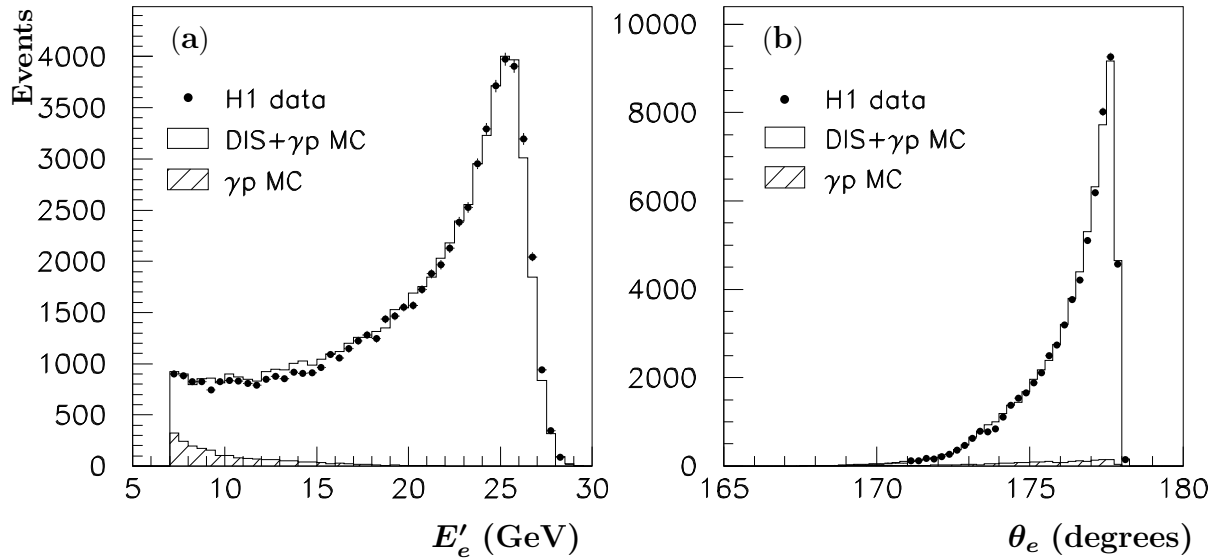


Figure 2: *Experimental (points) and Monte Carlo (solid histograms) distributions of a) the energy of the scattered electron and b) the polar angle of the scattered electron for DIS events. The Monte Carlo curves are the sum of DIS and photoproduction events and the photoproduction events alone.*

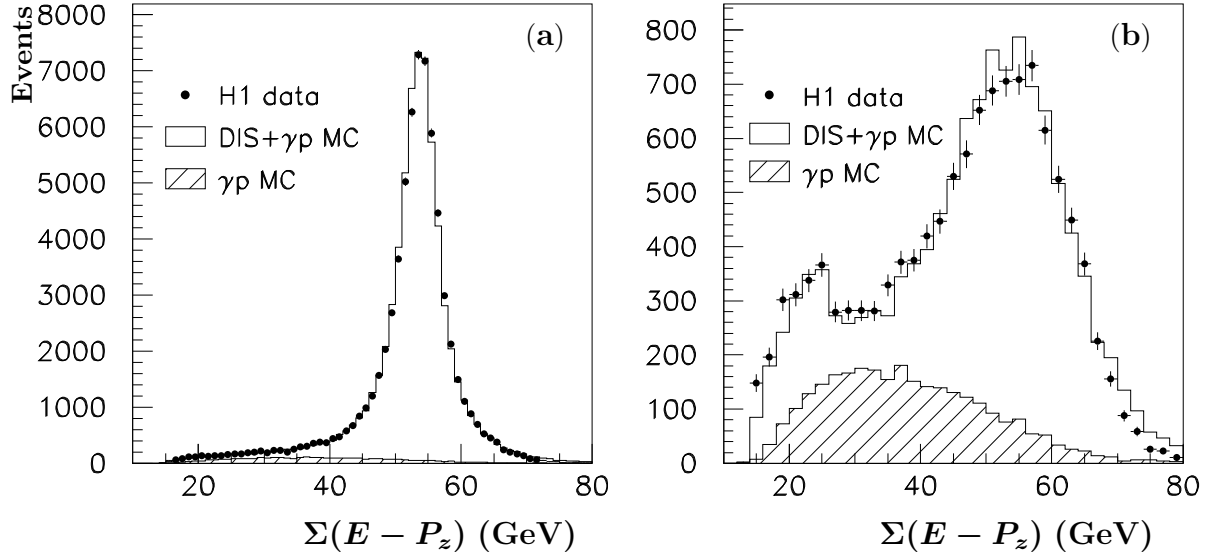


Figure 3: Experimental (points) and Monte Carlo (solid histograms) distributions of  $\Sigma(E_i - P_{z,i})$  measured in the calorimeter for a) all DIS event candidates and b) DIS event candidates with  $y_e > 0.55$ . The Monte Carlo curves are the sum of DIS and photoproduction events and the photoproduction events alone.

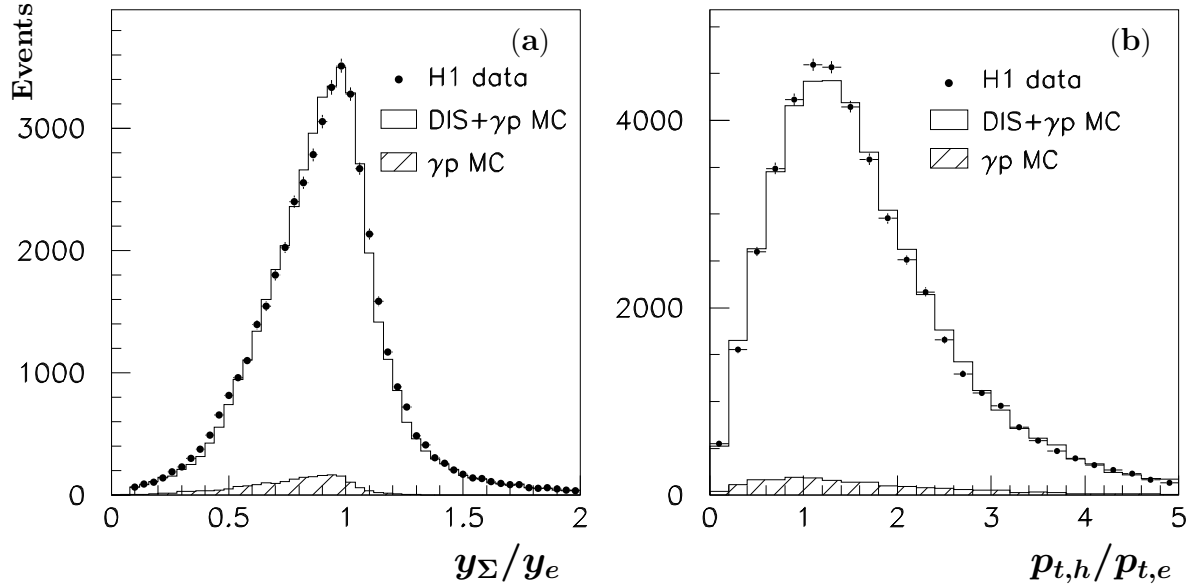


Figure 4: Experimental (points) and Monte Carlo (solid histograms) distributions for  $y_\Sigma > 0.05$  of the ratios of a) the  $y$  values measured with the  $\Sigma$  and  $E$  method  $y_\Sigma/y_e$ , and b) the transverse momentum of the hadronic system and the electron  $p_{t,h}/p_{t,e}$ . The Monte Carlo curves are the sum of DIS and photoproduction events and the photoproduction events alone.

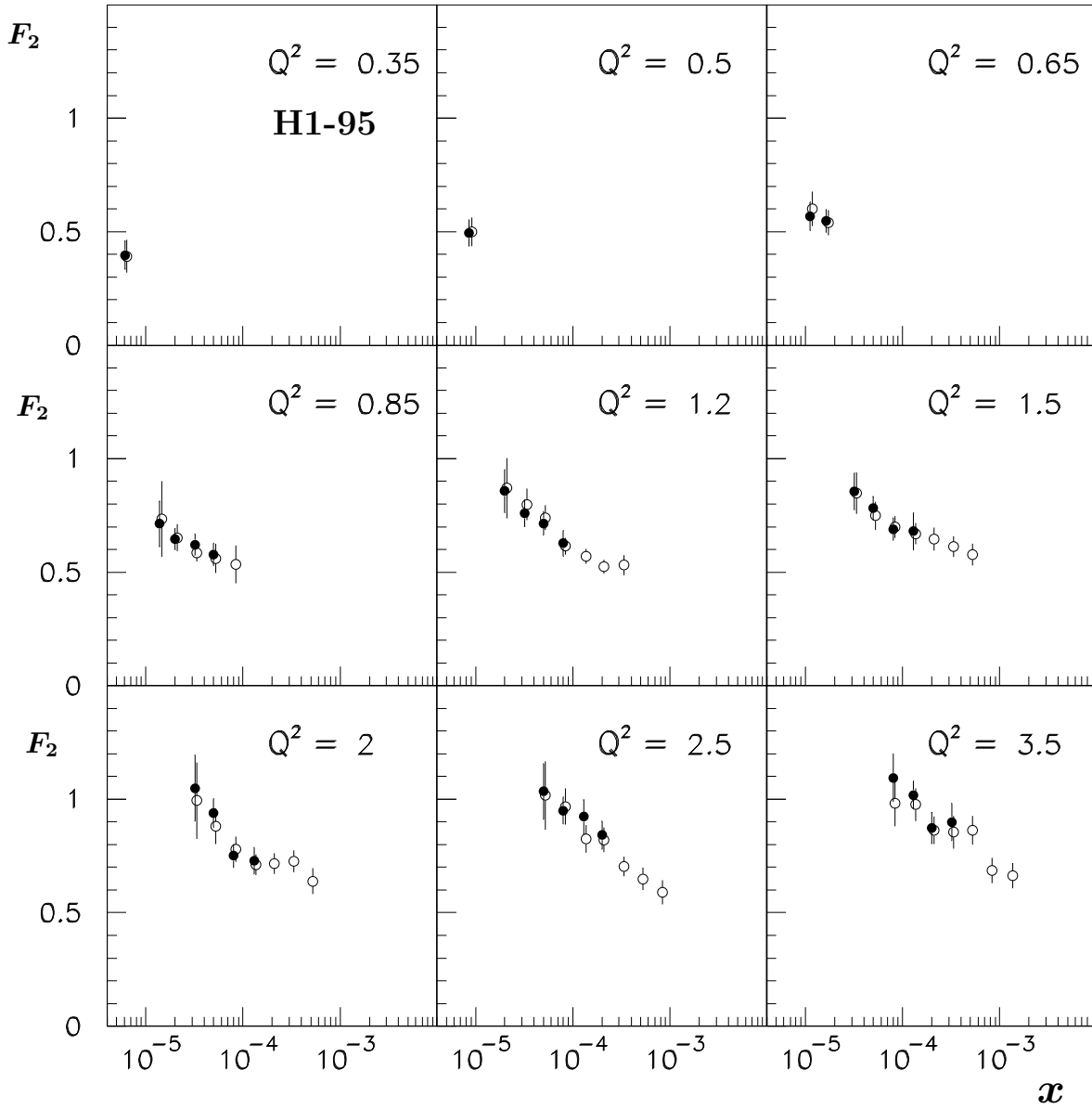


Figure 5: Comparison of the proton structure function  $F_2(x, Q^2)$  as a function of  $x$  at various values of  $Q^2$  (in  $\text{GeV}^2$ ) measured with the  $E$  method (full points) and with the  $\Sigma$  method (open points). The errors represent the statistical and systematic errors added in quadrature. A global normalization uncertainty of 3% is not included.

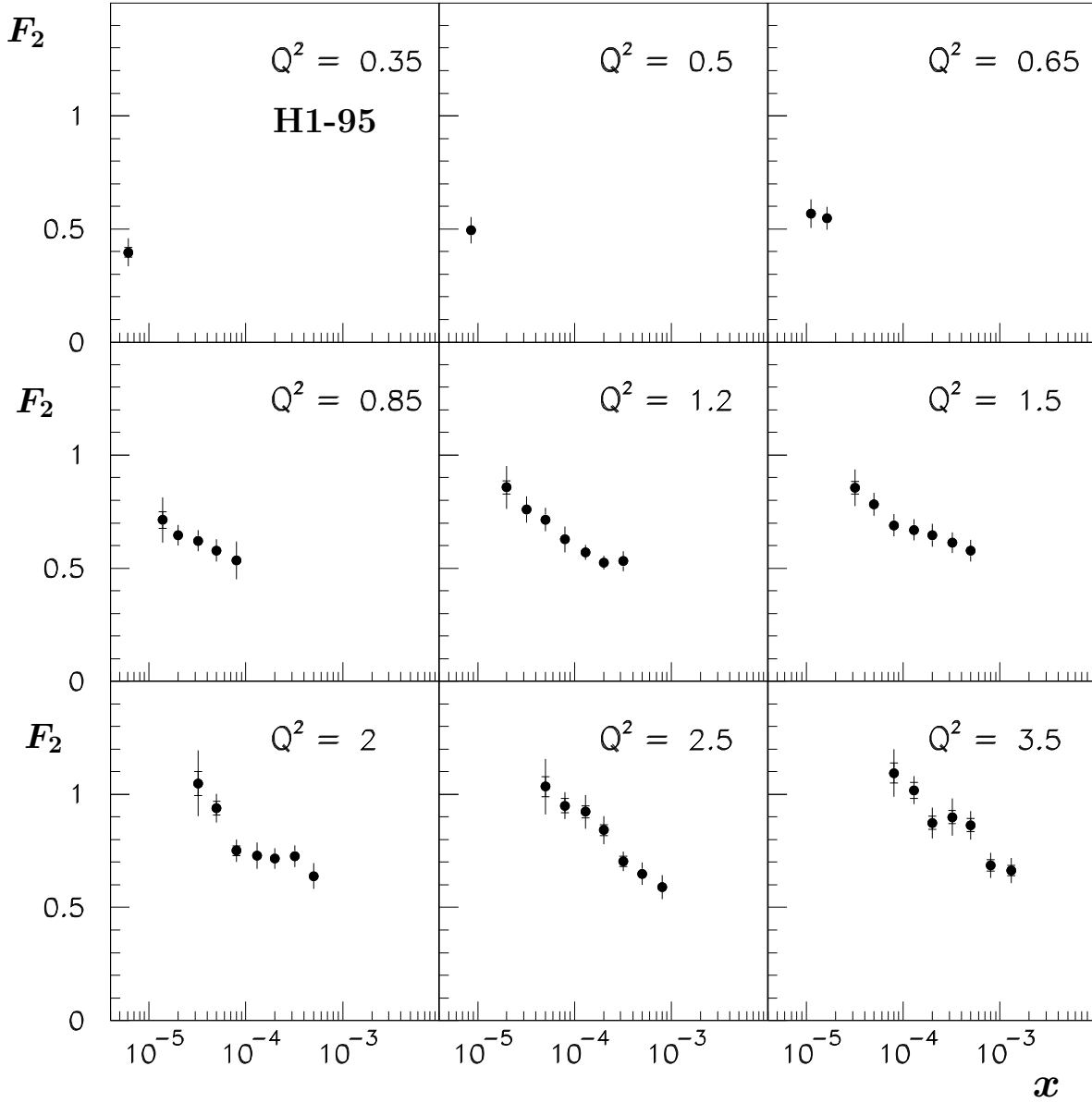


Figure 6: Measurement of the proton structure function  $F_2(x, Q^2)$  as a function of  $x$  at various values of  $Q^2$  (in  $\text{GeV}^2$ ). The inner error bars are the statistical errors, the outer error bars represent the statistical and systematic errors added in quadrature. A global normalization uncertainty of 3% is not included.



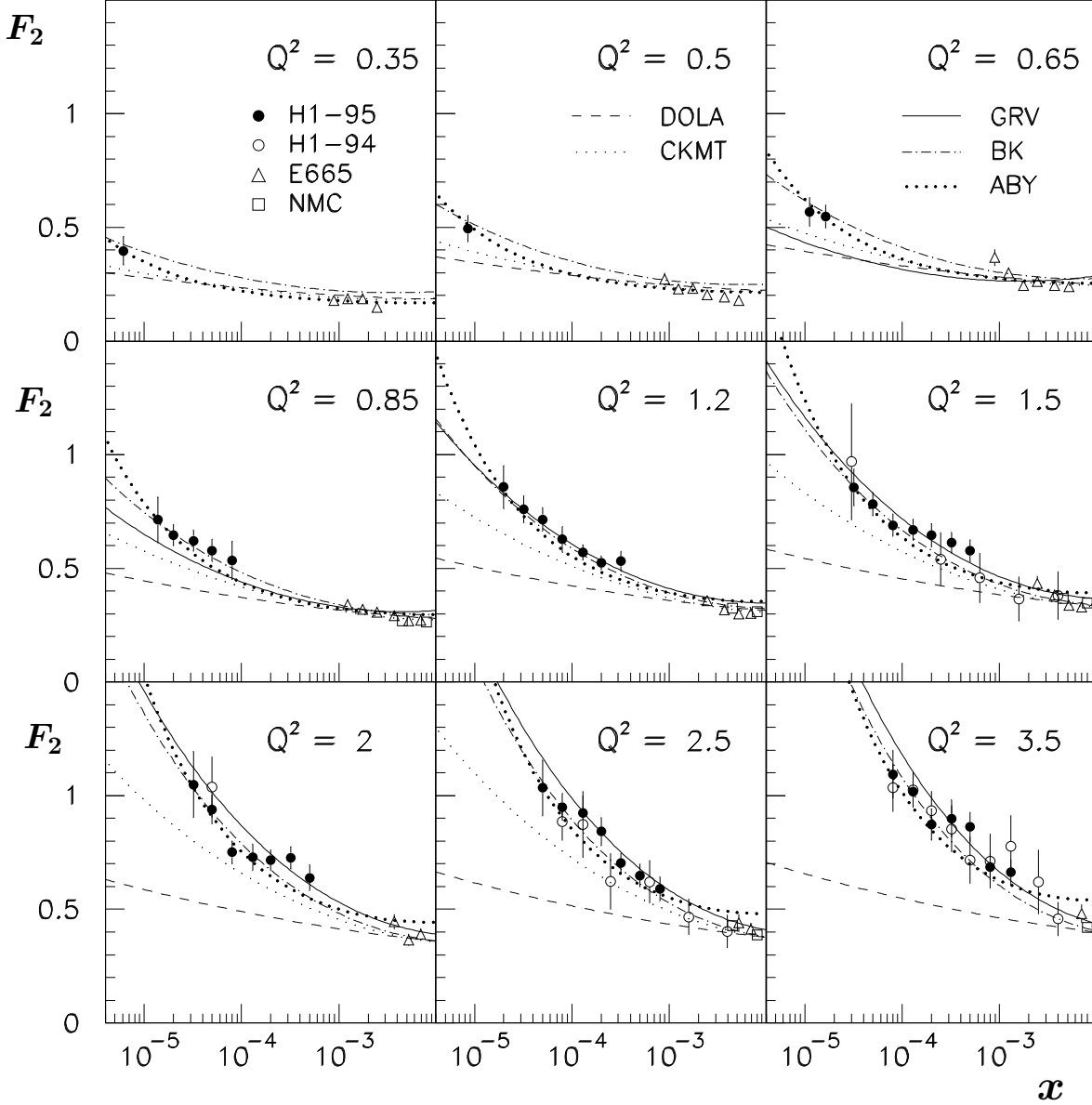


Figure 7: Measurement of the proton structure function  $F_2(x, Q^2)$  in the low  $Q^2$  region by H1 (full points), together with previously published results from H1 (open circles), E665 (open triangles), NMC (open squares). The  $Q^2$  values are given in  $\text{GeV}^2$ . Various predictions for  $F_2$  are compared with the data: the model of Donnachie and Landshoff (dashed line), the model of Capella et al. (dotted line/small), the model of Badelek and Kwiecinski (dashed-dotted line), the model of Glück, Reya and Vogt (full line) and the model of Adel et al. (dotted line/large). Global normalization uncertainties are not included.

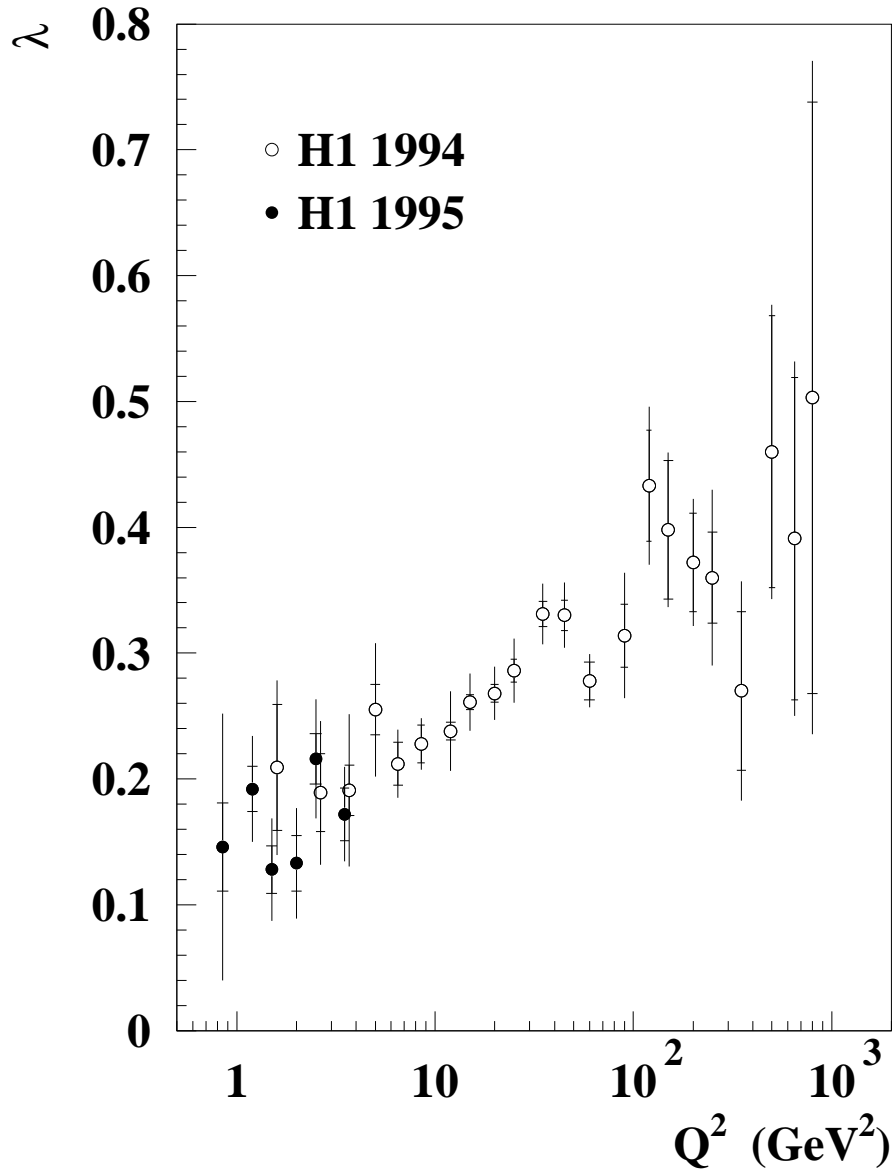


Figure 8: Variation of the exponent  $\lambda$  from fits of the form  $F_2 \sim x^{-\lambda}$  at fixed  $Q^2$  values and  $x < 0.1$ . Full symbols are the data from this analysis; open symbols are the data from [2]. The inner errors are statistical, and the full errors represent the statistical and systematic errors added in quadrature.

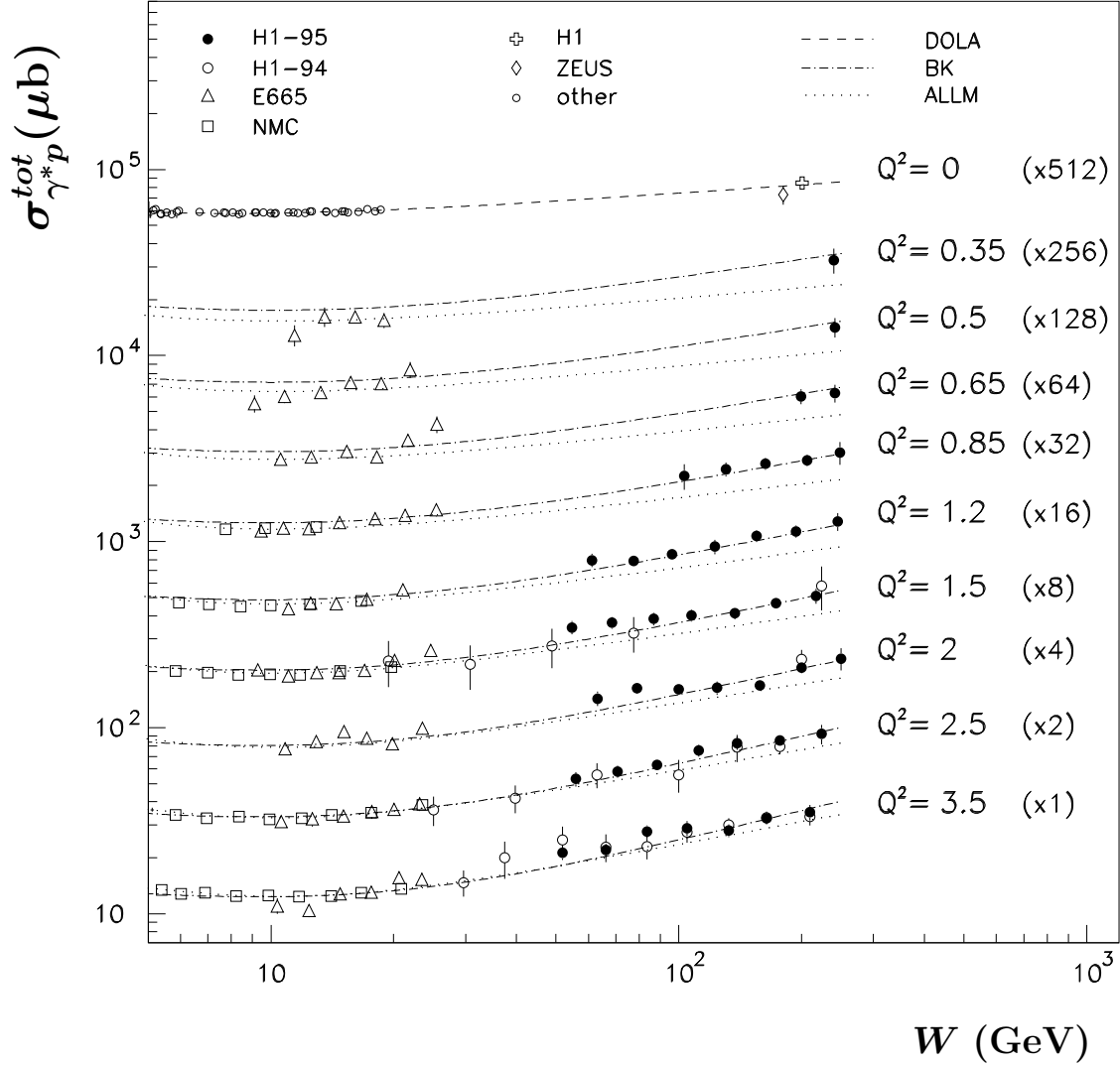


Figure 9: Measurement of the total virtual photon-proton cross section  $\sigma_{\gamma^*p}^{tot}$  as a function of  $W$  at various values of  $Q^2$  (in  $\text{GeV}^2$ ). The cross sections are multiplied with the factors indicated in the figure (numbers in brackets). The errors represent the statistical and systematic errors added in quadrature. Full symbols are data from this analysis; open symbols are previously published data from H1 (circles), E665 (triangles) and NMC (squares). Global normalization uncertainties are not included. The curves represent the DOLA (dashed line, only shown for  $Q^2 = 0$ ), ALLM (dotted line) and BK (dashed-dotted) parameterizations.

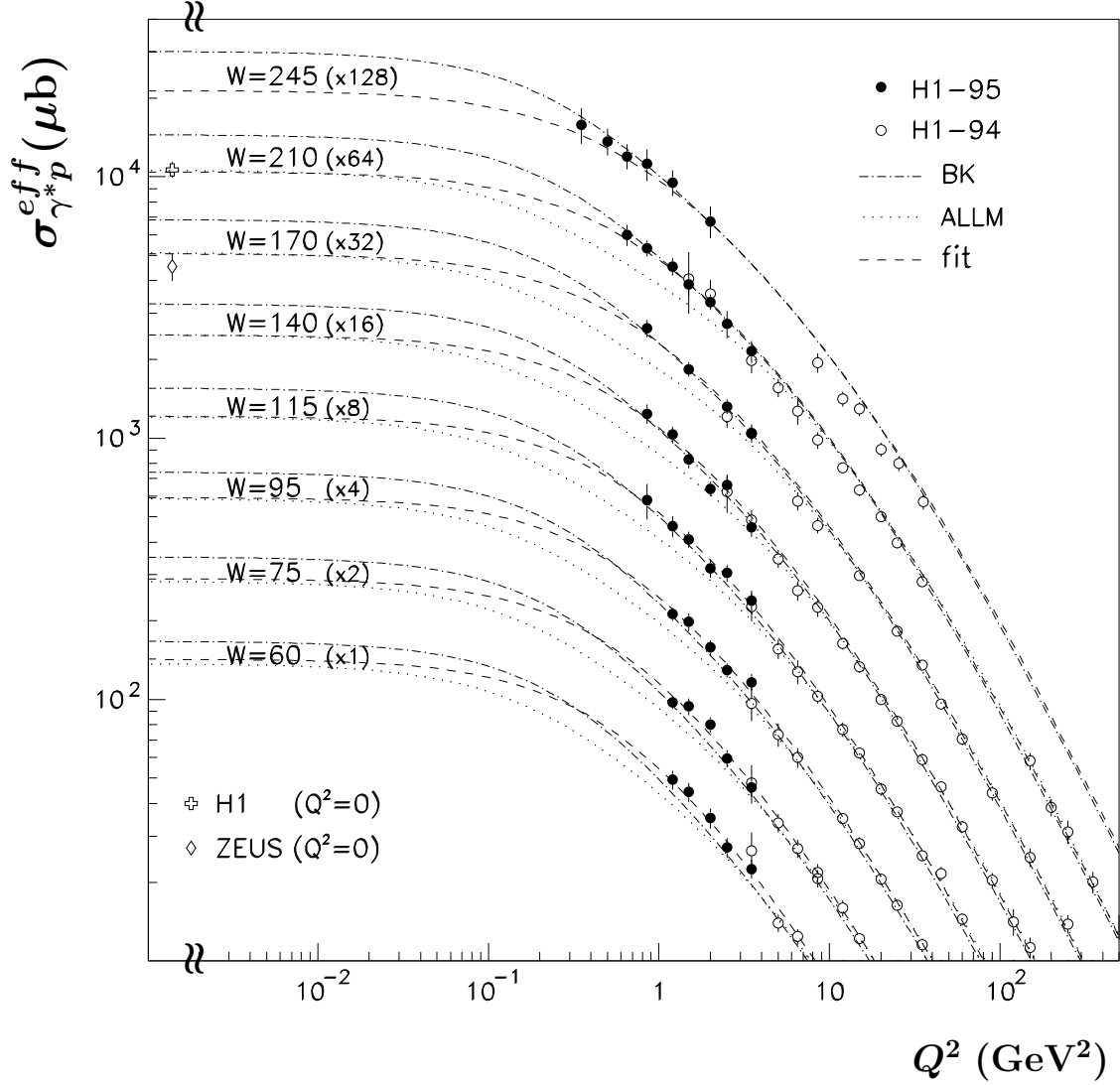


Figure 10: Measurement of the virtual photon-proton cross section  $\sigma_{\gamma^*p}^{eff}$  as a function of  $Q^2$  at various values of  $W$  (in GeV). The cross sections for consecutive  $W$  values are multiplied with the factors indicated in the figure (numbers in brackets). The errors represent the statistical and systematic errors added in quadrature. Full symbols are data from this analysis; open symbols are H1 data from [2, 4]. The photoproduction points (cross:  $W = 210$  GeV, diamond:  $W = 170$  GeV) are from [6, 7]. Global normalization uncertainties are not included in the errors shown. The curves represent the ALLM (dotted line) and BK (dashed-dotted line) parameterizations and the H1 fit based on BK (dashed line).